School of Mathematics & Statistics

MAS8091: MMath Project

Neutral Hydrogen In The Milky Way

Written By:
Neil Wilyman

Supervised By:
Dr. Andrew Fletcher

May 2014

Abstract

Neutral atomic hydrogen (HI) comprises most of the gas in our Galaxy, the Milky Way. The associated 21cm emission line, measured using a radio telescope, allows detection of HI. Using the radio telescope, SALSA, data has been collected and hence used to identify properties of observed HI gas clouds in the Galaxy. These properties are used to derive a rotation curve for the Galaxy, showing the relationship between Galactic radius and rotational velocity of the clouds, in the Galactic plane. From this rotation curve models of the distribution of the gravitating mass in the Galaxy can be derived. The rotation of the gas outside of the Galactic plane is also of interest and can be deduced from 21cm observations. Using the observations smaller movements are also examined, such as the random turbulent motions within HI gas clouds which are rotating around the Galactic centre.

Contents

Chapter 1

The Milky Way

This report is concerned with gathering data about our own galaxy, the Milky Way, and using this data to infer properties about it. The Galaxy contains about 10^{11} visible stars and that most of these lie in a flattened, roughly axisymmetric, disc-like structure known as the Galactic disc. The radius of this disc is given to be of order 10 kpc. To describe a position in the Galaxy we use the Galactic coordinate system, (l, b), where l is the Galactic longitude and b the Galactic latitude, shown in Figure 1.1. This system is centered at the Sun. The longitude is measured counterclockwise from the Galactic centre, where $l = 0°$. When $b = 0°$ we are said to be in the Galactic plane. The Galactic centre thus lies on the line of sight $(l, b) = (0°, 0°)$.

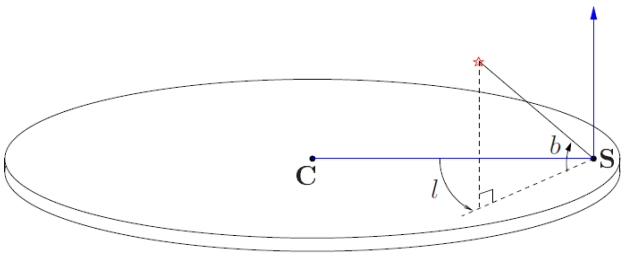

Figure 1.1: Illustration of the Galactic coordinate system, showing longitude and latitude coordinates, (l, b). C indicates the position of the Galactic centre, and S the position of the Sun. (Horellou and Johansson, 2013, Fig 1.1).

The distance between the Sun and the Galactic centre is denoted R_0. The current estimate is $R_0 = 8.5 \pm 1$ kpc, (Binney and Tremaine, 1987), this is the so-called solar radius. The stars in the Galactic disc travel in approximately circular orbits around the Galactic centre. The circular velocity of the Sun, denoted V_0, has current estimate $V_0 = 220 \pm 15$ km/s, (Binney and Tremaine, 1987). We adopt these values.

When making observations in the Galactic plane it is convenient to split this into four quadrants. These are shown, along with the assumed Galactic constants R_0 and V_0, in Figure 1.2.

A detailed artist's impression showing the currently believed structure of the Milky Way is shown in Figure 1.3. We see the flat Galactic disc in the Galactic plane. We also note the shape taken by the stars in spiral arms around the Galactic centre.

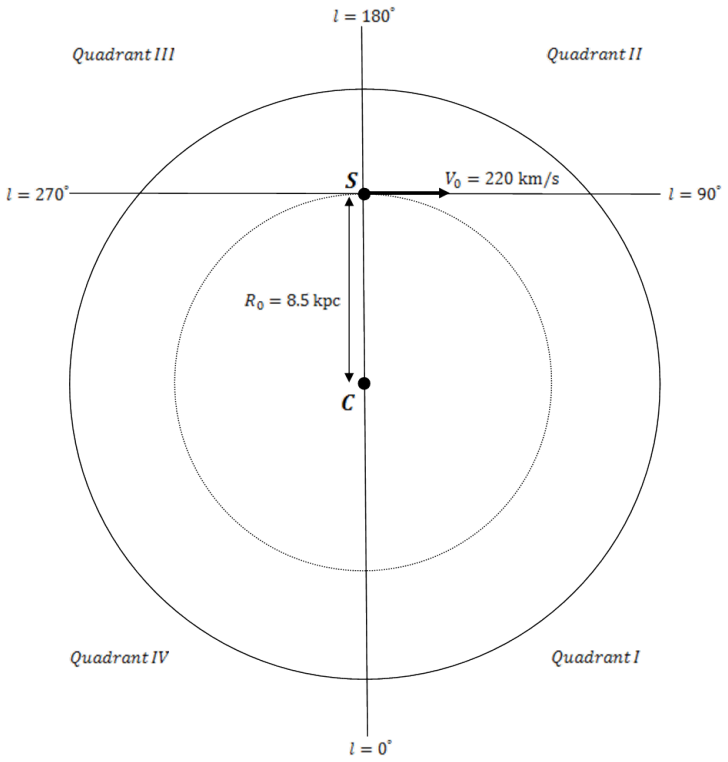

Figure 1.2: Schematic showing the Galactic plane, $b = 0°$. C indicates the position of the Galactic centre and S the position of the Sun. Quadrant labels are shown as well as astronomical constants R_0 and V_0.

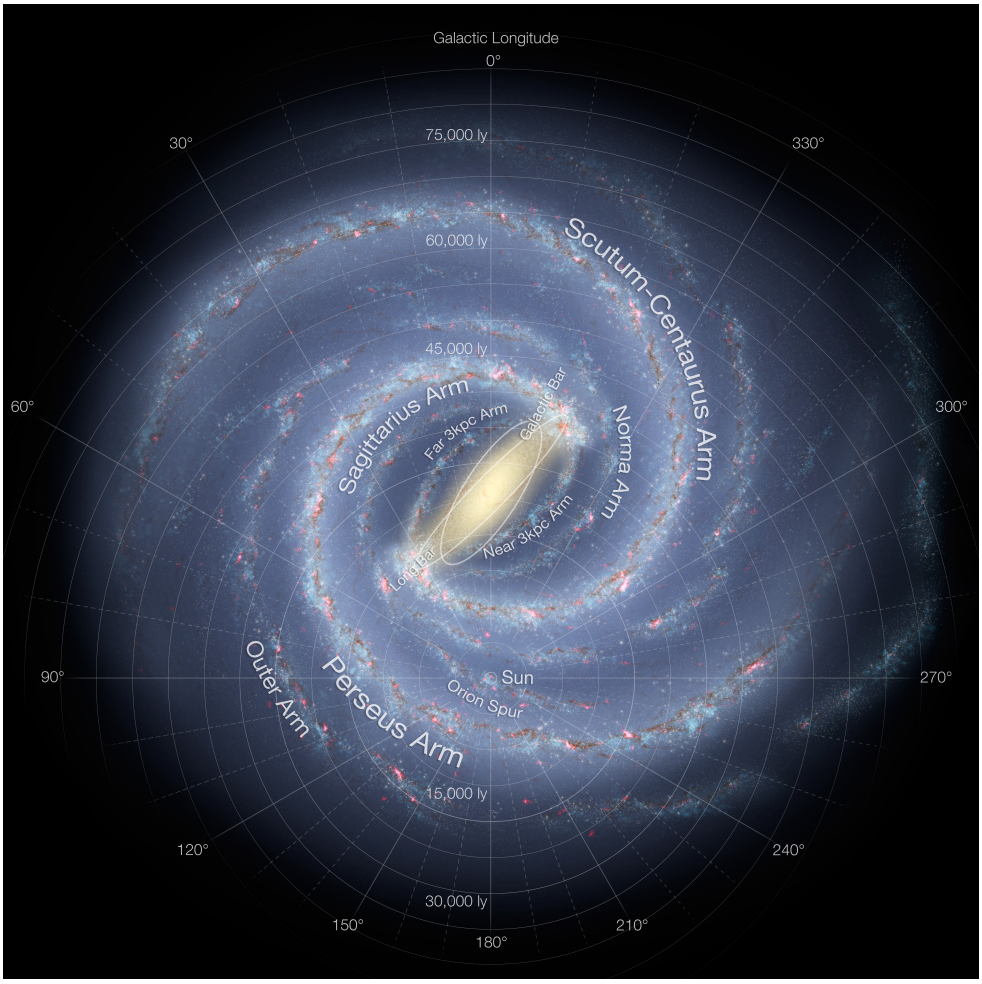

Figure 1.3: Annotated artist's impression of the Milky Way. Obtained from solarsystem.nasa.gov.

Chapter 2

Potential Theory

We start with **Newton's law of universal gravitation**, (Cohen and Whitman, 1999), which states that: "Any two bodies in the universe attract each other with a force that is directly proportional to the product of their masses and inversely proportional to the square of the distance between them." This gives

$$F = G\frac{m_1 m_2}{r^2}, \tag{2.1}$$

where

- F is the force between the masses,
- G is the gravitational constant,
- m_i, for $\{i \in 1, 2\}$, are the respective masses, and
- r is the distance between the centers of the masses.

Here we calculate the force $\mathbf{F}(\mathbf{x})$ on a unit mass, at position $\mathbf{x}$, that is generated by the gravitational attraction of a distribution of mass $\rho(\mathbf{x})$, as outlined by Binney and Tremaine (1987). $\mathbf{F}(\mathbf{x})$ can be obtained by summing over all the small contributions of the overall force from each small element of the volume, $\delta^3\mathbf{x}'$, located at $\mathbf{x}'$. Applying this using Newton's law of gravitation we obtain

$$\delta\mathbf{F}(\mathbf{x}) = G\frac{(1)\cdot\delta m(\mathbf{x}')}{|\mathbf{x}'-\mathbf{x}|^2} = G\frac{\rho(\mathbf{x}')\delta^3\mathbf{x}'}{|\mathbf{x}'-\mathbf{x}|^2} = G\frac{\mathbf{x}'-\mathbf{x}}{|\mathbf{x}'-\mathbf{x}|^3}\rho(\mathbf{x}')\delta^3\mathbf{x}',$$

which when summed over all small elements becomes

$$\mathbf{F}(\mathbf{x}) = G\int \frac{\mathbf{x}'-\mathbf{x}}{|\mathbf{x}'-\mathbf{x}|^3}\rho(\mathbf{x}')d^3\mathbf{x}'.$$

Defining the **gravitational potential**, $\Phi(\mathbf{x})$, to be

$$\Phi(\mathbf{x}) = -G\int \frac{\rho(\mathbf{x}')}{|\mathbf{x}'-\mathbf{x}|}d^3\mathbf{x}',$$

and noting that

$$\nabla\left(\frac{1}{|\mathbf{x}'-\mathbf{x}|}\right) = \frac{\mathbf{x}'-\mathbf{x}}{|\mathbf{x}'-\mathbf{x}|^3},$$

we can write

$$\mathbf{F}(\mathbf{x}) = \nabla\int \frac{G\rho(\mathbf{x}')}{|\mathbf{x}'-\mathbf{x}|}d^3\mathbf{x}' = -\nabla\Phi. \tag{2.2}$$

An expression for the gravitational force on a mass in terms of the gravitational potential.

Within a spherically symmetric system, **Newton's second theorem** can be applied (Binney and Tremaine, 1987, p.34). This states that: "The gravitational force on a body that lies outside a closed spherical shell of matter is the same as it would be if all the shell's matter were concentrated at a point at its centre."

Using this and the law of universal gravitation we have that the directional force, $\mathbf{F}$, of a gravitational attraction on a unit test mass at radius R is determined by the mass interior to R, given by

$$\mathbf{F}(R) = -\frac{GM(R)}{R^2}\hat{\mathbf{e}}_\mathbf{r} = -\frac{d\Phi}{dR}\hat{\mathbf{e}}_\mathbf{r}. \tag{2.3}$$

using Eq. (2.2).

For particle of mass m at radius R to be in orbit around a central mass with distribution $M(R)$ at speed $V(R)$, we require that the sizes of the centrifugal force and the gravitational force be in balance. Hence we have

$$\begin{aligned} |\text{Centrifugal Force}| &= |\text{Gravitational Force}| \\ \Rightarrow \quad \frac{mV^2(R)}{R} &= \frac{GM(R)m}{R^2} \\ \Rightarrow \quad V^2(R) &= \frac{GM(R)}{R} = R\frac{d\Phi}{dR}. \end{aligned} \tag{2.4}$$

Using this equation we can relate the rotational velocity of an orbiting mass in the galaxy to its distance from the Galactic centre, if we know either the gravitational potential or mass distribution.

From the general result obtained in Eq. (2.2) the following useful relations involving the gravitational potential can also be derived, (Binney and Tremaine, 1987).

Poisson's Equation, this relates the potential to the density, ρ, and is given by

$$\nabla^2\Phi = 4\pi G\rho. \tag{2.5}$$

Laplace's Equation, this is a special case of Poisson's equation, with $\rho = 0$, and is given by

$$\nabla^2\Phi = 0. \tag{2.6}$$

Chapter 3

Data Collection

3.1 Hydrogen, the 21cm Line and the Doppler Shift

Most of the gas in the Galaxy is atomic hydrogen. Neutral atomic hydrogen, HI, emits radiation at a wavelength of $\lambda = 21$cm, this arises because the proton and the electron both poses a spin and a magnetic moment; if the spins change from being parallel to anti-parallel a photon with 21cm wavelength is emitted (Tayler, 1993). This wavelength corresponds to a frequency of approximately 1420 MHz and was first detected by Ewen and Purcell (1951). This electromagnetic energy can easily pass through the Earth's atmosphere and hence be observed with little interference using a radio telescope.

When observations are made in a specific direction the radiation does not all appear at 21cm. This is due to Doppler shifts arising because the gas cloud as a whole is moving towards or away from us, hence shifting the observed frequency. Therefore using knowledge of the Doppler shift the velocity of the observed cloud in the given direction can be calculated.

3.2 SALSA - 'Such a Lovely Small Antenna'

SALSA is a small antenna (2.3m in diameter) situated at the Onsala Space Observatory, which is located 45 km south of Gothenburg in Sweden, shown in Figure 3.1. There are two observing antennas which are used separately, also shown in Figure 3.1. These are used to observe the spectral line from neutral hydrogen corresponding to the 21cm wavelength and hence to calculate the velocity of observed Galactic clouds from the Doppler shift.

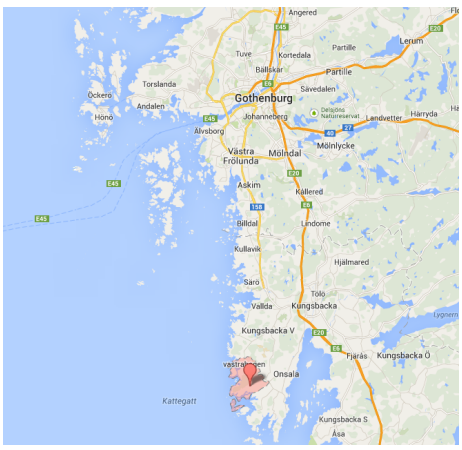

Figure 3.1: Left: Map showing the location of the Onsala Space Observatory - obtained from Google Maps. Right: Photograph of the two SALSA telescopes - obtained from the SALSA website.

Controlling SALSA over the Internet I made observations of the HI clouds in the Galaxy. To do this you first access the SALSA computer remotely and run the program Q-Radio. The 'Frequency/Gain' should be controlled to adjust the associated 'Power' to be approximately 30%, this represents the value needed for the specific receiver used for SALSA The "Power" is continuously changing as the antenna moves and therefore needs to be adjusted for each observation. A position is then specified, in Galactic longitude and latitude (l, b), and this is then found and tracked by SALSA; using the live webcam you can see the antenna moving to the specified position. Once the position is being tracked you can make an observation. I observed on the specified line of sight (LOS) for 30 seconds per observation, a strong signal is recorded after only 10 seconds however observing for a longer time reduces the background noise; 30 seconds gives a spectrum with minimal noise and without taking a long time to observe.

Observations have been taken in the Galactic plane ($b = 0°$) for $0° \leq l \leq 210°$ with $5°$ increments in l. Owing to the location of Onsala I could not observe at any other Galactic longitudes since these are never visible. Observations have also been made for fixed longitude, $l = 80°$, and $-30° \leq b \leq 30°$, with $2°$ increments in b. For each LOS between 3 and 5 observations were made to enable me to find averages in analysis, as well as uncertainty. Details of the dates of all observations are shown in Appendix A.

The observation data are in the form of '.FITS' files which were analysed using Matlab with the manual and program provided by Dahlin (2013) used as a guide. Emission spectra were obtained for each observation, one example is shown in Figure 3.2.

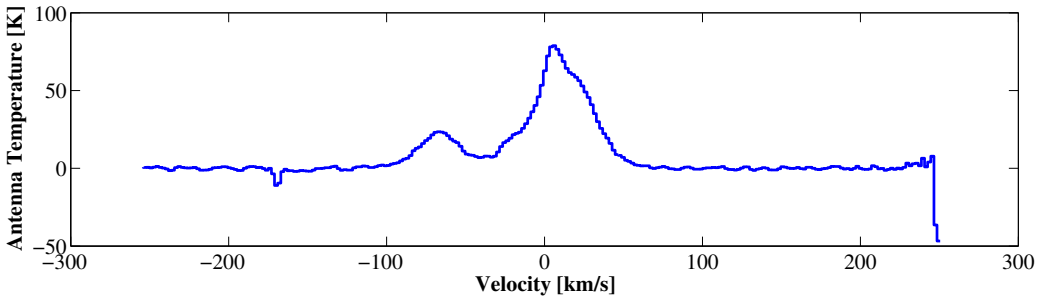

Figure 3.2: Observed emission spectrum for $(l, b) = (60°, 0°)$ showing two peaks corresponding to two clouds emitting 21cm radiation.

Using Dahlin's program Gaussian curves were fitted to observed peaks, as shown in Figure 3.3. We note that any negative "Antenna Temperature" readings were assumed to be 'noise' and are hence ignored.

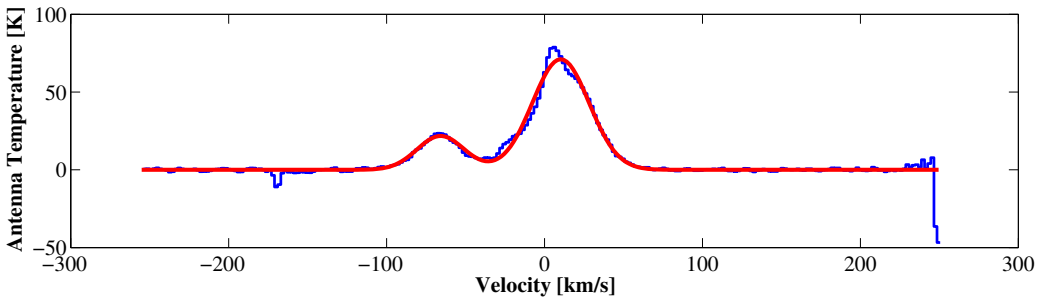

Figure 3.3: Observed emission spectrum for $(l, b) = (60°, 0°)$ with two fitted Gaussians.

From each Gaussian we obtained three pieces of information, shown in Table 3.1. The 'Antenna Temperature' tells us the strength/intensity of the signal. The 'Velocity' is the observed clouds velocity along the LOS, this is called the radial velocity. The 'Standard Deviation' is a measure of the width of the Gaussian caused by random motions inside the clouds.

	Antenna Temperature [K]	Velocity [km/s]	Standard Deviation [km/s]
Gaussian 1	71.1	10.3	18.0
Gaussian 2	21.8	-65.8	14.8

Table 3.1: Observed parameters for fitted Gaussians for the spectrum for $(l, b) = (60°, 0°)$, shown in Figure 3.3.

This information has been obtained for each peak in all observed spectra as well as averages and standard deviations found for the multiple observations on each LOS. For constant latitude, $b = 0°$, and varied longitude, $0° \leq l \leq 210°$, all values can be found in Appendix B. Similarly for constant longitude, $l = 80°$, and varied latitude, $-30° \leq b \leq 30°$, all values can be found in Appendix C. This information will be used in analysis.

For comparison we now look at a spectrum found by McClure-Griffiths et al. (2009) in the Parkes Galactic All-Sky Survey (GASS). GASS is the most sensitive, highest angular resolution survey of Galactic HI emission ever made in the southern sky.

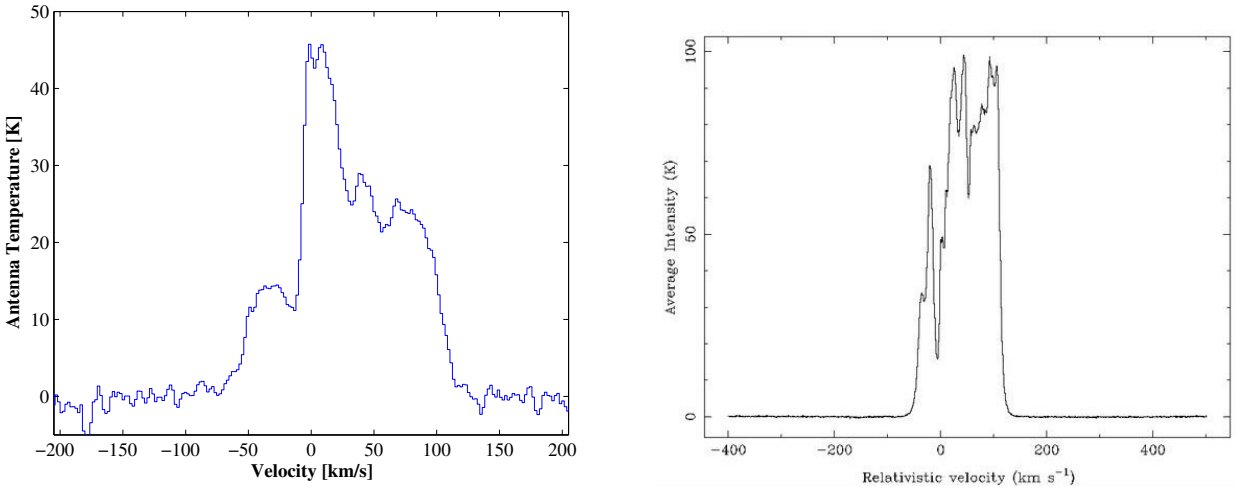

Figure 3.4: Both spectra are observed from the LOS with $(l, b) = (30°, 0°)$. Left: My observed spectrum from SALSA. Right: Spectrum from the Parkes GASS.

The Parkes telescope has a diameter of 64m, compared to SALSAs 2.3m: thus we see the spectrum from the GASS has considerably higher spectral resolution and also receives a much stronger signal with observed temperature up to 100 K whereas the SALSA spectrum has weaker intensity, less than 50 K. Therefore peaks are much more clearly defined on the GASS spectrum. However for the location of observed peaks the spectra show a close resemblance. We observe a peak at the left at approximately $V = -20$ km/s, a double peak at approximately $V = 40$ km/s and further peaks identifiable for larger V. This is true for both spectra.

Chapter 4

Rotation Curves

Using SALSA we observed the radial velocities of hydrogen clouds at a range of Galactic positions. For this analysis only spectra observed in the Galactic plane, $b = 0°$, are analysed. We now obtain the rotation curve, thus showing the relationship between the distance from the Galactic centre and the rotational velocity. To do this we follow the procedure laid out in the manual provided by SALSA, (Horellou and Johansson, 2013).

4.1 Preliminary Calculations

In this section some general results are derived for the whole Galactic plane. Using these the observed radial velocity (V_r), and Galactic longitude and latitude (l, b) are converted into a circular velocity (V) and a Galactic radius (R), within the Galactic plane. To do this we make use of the geometry of the Galaxy, shown in Figure 4.1.

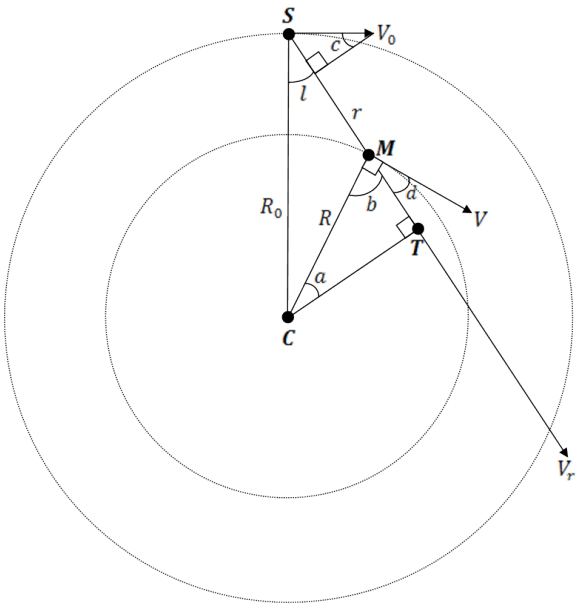

Figure 4.1: The geometry of the Galaxy for a gas cloud observed in the Galactic plane. Where S is the Sun, C is the Galactic centre and M is the position of the observed cloud. Distances shown are R_0, R and r and velocities shown are V_0, V and V_r. Angles of interest are labeled $a - d$ and l, where l is the Galactic longitudinal coordinate. Reproduced from Horellou and Johansson (2013).

Note that: the values, $V_0 = 220$ km/s and $R_0 = 8.5$ kpc, are assumed to be known; the distance, r, between the Sun, S, and the observed cloud, M, is unknown; and the following formulae have been derived using a schematic for Quadrant I of the Galaxy, however they hold everywhere in the Galactic plane.

4.1.1 Rotational Velocity

A cloud's radial velocity is measured on the LOS and is hence the difference between its rotational velocity and the velocity of the Sun, both projected onto the LOS. Using Figure 4.1, we obtain

$$V_r = V\cos(d) - V_0\sin(c). \tag{4.1}$$

Using the upper most triangle we see that

$$(90 - l) + 90 + c = 180 \quad \Rightarrow \quad c = l,$$

from the triangle CMT we have

$$a + b + 90 = 180 \quad \Rightarrow \quad b = 90 - a,$$

and the right angle the line CM makes with V gives

$$b + d = 90 \quad \Rightarrow \quad d = 90 - b = 90 - (90 - a) = a.$$

Hence Eq. (4.1) becomes

$$V_r = V\cos(a) - V_0\sin(l). \tag{4.2}$$

Looking at the triangles CMT and CST we define the distance CT in two equivalent ways, given respectively by $CT = R\cos(a)$ and $CT = R_0\sin(l)$, therefore

$$\cos(a) = \frac{R_0}{R}\sin(l).$$

Hence substituting this into Eq. (4.2) we obtain

$$V_r = V\frac{R_0}{R}\sin(l) - V_0\sin(l),$$

yielding the following general formula for the rotational velocity

$$V = \frac{R}{R_0}\left[\frac{V_r + V_0\sin(l)}{\sin(l)}\right]. \tag{4.3}$$

4.1.2 Galactic Radius

The distance of a cloud from the Galactic centre, R, can be obtained by applying the cosine rule to the triangle CSM, remembering that the distance SM is of length r, giving

$$R = \sqrt{r^2 + R_0^2 - 2rR_0\cos(l)}. \tag{4.4}$$

Note that Eq. (4.4) can be rearranged to give a formula for the distance between us and the cloud, r. Also note that we take only the positive square root since R is a distance and must be positive.

4.2 Rotation Curve Inside The Solar Radius

In this section we derive the rotation curve from observations of the 1st Galactic Quadrant ($0° \leq l \leq 90°$) and for clouds which are inside the solar radius, $R < R_0$.

Multiple peaks in Figure 3.2 show that several clouds may exist along one LOS. This can also be seen in Figure 4.1 as any LOS crosses many circular orbits. We assume that the largest observed radial velocity, the furthest right in the spectrum, $V_{r,max}$, comes from a cloud at the tangential point (T), where we observe the whole velocity vector along the LOS. Only clouds assumed to be at the tangent points will be used to derive $V(R)$. This gives a simplified schematic of the geometry of the Galaxy, shown in Figure 4.2.

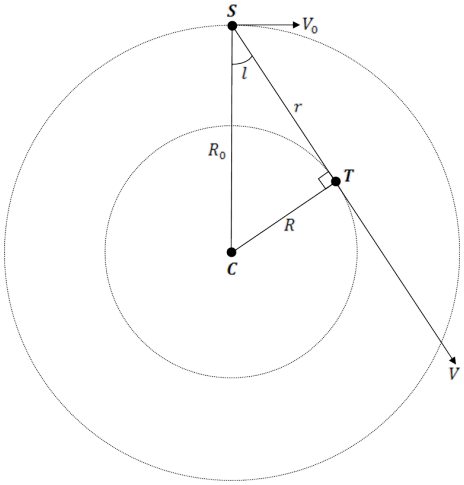

Figure 4.2: The geometry of the Galaxy for a gas cloud at the tangential point, T, with distances and angles of interest defined as in Figure 4.1. Notice here that V_r and V are both directed on the LOS. Reproduced from Horellou and Johansson (2013).

From inspection of triangle CST

$$R = R_0 \sin(l). \tag{4.5}$$

Alternatively this can be found by noting, also using triangle CST, that $r = R_0 \cos(l)$, and substituting this into Eq. (4.4) for the same result. This expression for R simplifies Eq. (4.3), giving the rotational velocity of a cloud at the tangential point

$$V = V_{r,max} + V_0 \sin(l). \tag{4.6}$$

Using the data from the observed spectrum in Figure 3.3 as an example, first $V_{r,max}$ is identified from the spectrum, shown in Figure 4.3.

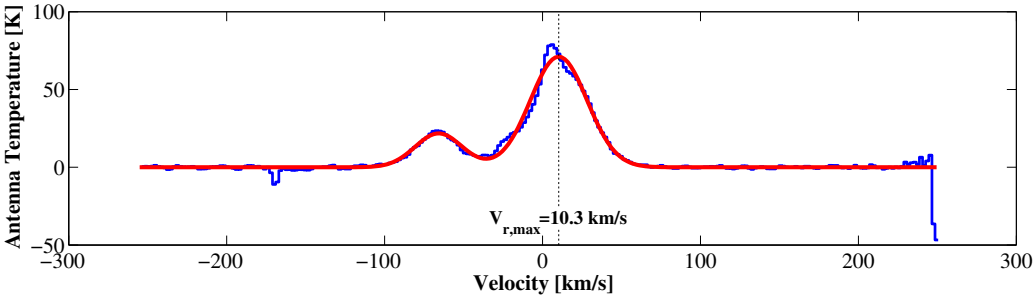

Figure 4.3: Reproduced Figure 3.3 with maximum velocity peak indicated.

Therefore for this observed cloud, from Eqs. (4.5) and (4.6), we have

$$R = 8.5\sin(60) = 7.4 \text{ kpc} \quad \text{and} \quad V = 10.3 + 220\sin(60) = 200.8 \text{ km/s}.$$

This observed cloud is 7.4 kpc from the Galactic centre and is orbiting the centre with rotational velocity 200.8 km/s.

For each LOS we have multiple observations of $V_{r,max}$, therefore we can find the mean and standard deviation of these observations and use these to find a confidence interval for our observed circular velocity.

For example at $(l, b) = (60°, 0°)$ we have

$$\bar{V}_{r,max} = 12.8 \text{ km/s} \quad \text{and} \quad \text{SD}(V_{r,max}) = 3.4 \text{ km/s}.$$

A 95% confidence interval for $V_{r,max}$ is given by $\bar{V}_{r,max} \pm 1.96 \times \text{SD}(V_{r,max})$, therefore we have

$$V_{r,max} = 12.8 \pm 6.7 \text{ km/s}.$$

Now applying Eq. (4.6) to the lower and upper values for $V_{r,max}$ as well as the average we obtain a 95% confidence interval for V. For $(l, b) = (60°, 0°)$ we have

$$V = 203.3 \pm 6.8 \text{ km/s}.$$

The rotation curve, derived from all observations, is shown in Figure 4.4. The plotted points are the average velocities of the multiple observations of $V_{r,max}$ along each LOS.

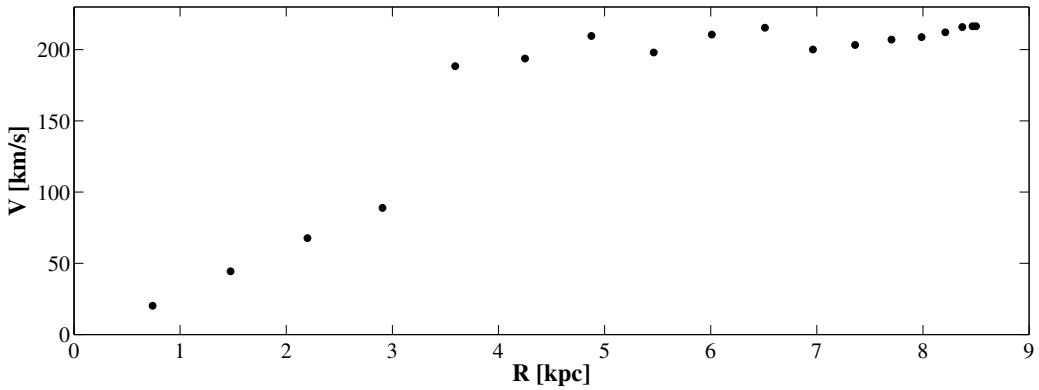

Figure 4.4: Rotation curve for all observations of $V_{r,max}$ inside the solar radius.

We can see that for $R > 3$ kpc we have an approximately flat rotation curve, with $V \simeq 200$km/s. The points at small radii do not follow this form of the rotation curve, this is likely to be because lines of sight close to the Galactic centre look through many more clouds making it difficult to select the V_r at the tangent point. It follows that the observed maximum peaks in the spectra may not come from clouds at tangential points, making our transformation formulae inaccurate. For this reason all points with $R < 3$ kpc are removed for all further analysis.

Figure 4.5 shows the associated 95% confidence intervals for the remaining observations. We note that this is the confidence associated with observational values only, not the systematic errors associated with the assumptions made in analysis. Error bars are all reasonably small in magnitude. This shows the Gaussian peaks for multiple observations all gave consistently similar values of observed radial velocities and hence a small standard deviation.

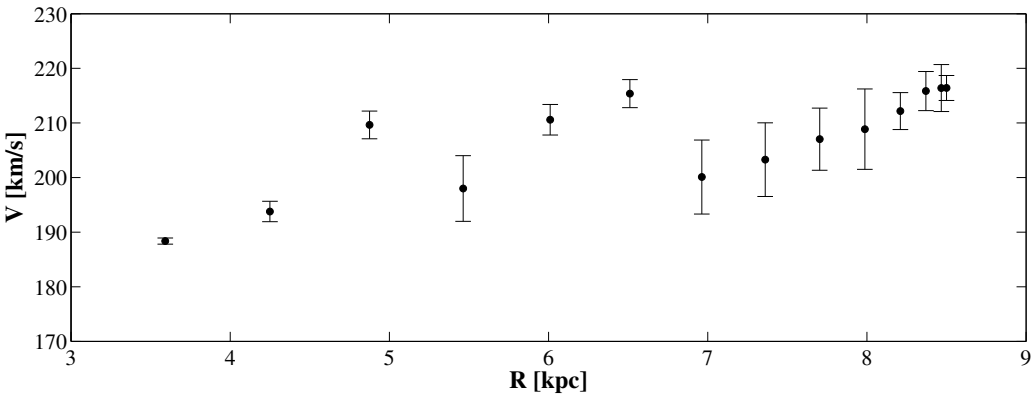

Figure 4.5: Reduced rotation curve with 95% confidence error bars over laid.

From these findings we conclude that the detected HI clouds follow an approximately constant rotation curve, shown in Figure 4.6. This is $V(R) = 207 \pm 4$ km/s, where 207 km/s is the average of all observed V, and the confidence interval is the average width of the intervals associated with each observation. For comparison, the flat rotation given by Sofue (2013) is $V(R) = 200 \pm 6$ km/s.

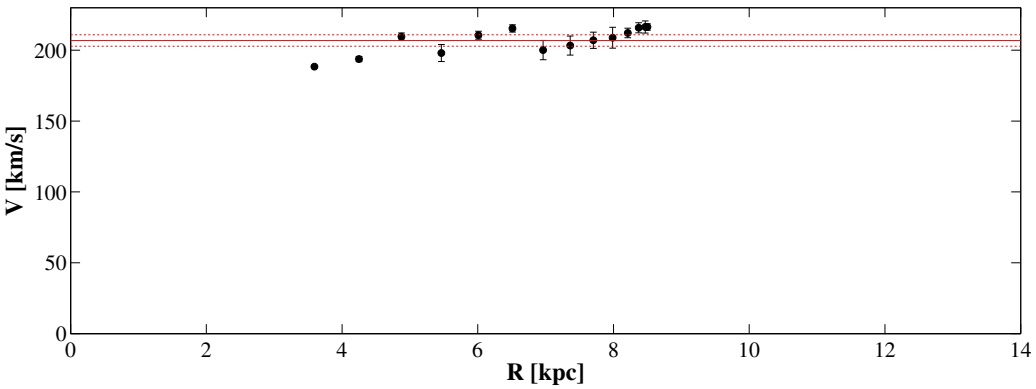

Figure 4.6: Equivalent points shown as in Figure 4.5 with average rotational velocity indicated, solid red line, and associated 95% confidence interval, dotted red line.

4.3 Rotation Curve Beyond The Solar Radius

In this section we will attempt to use the data to derive the rotation curve for Quadrants II and III ($90° < l \leq 270°$). The data collected includes only observations up to 210° Galactic longitude. In these two Quadrants the LOS can never be at a tangential point to the observed cloud, shown in Figure 4.7. Therefore Eqs. (4.5) and (4.6) do not hold here.

Therefore we return to Eqs. (4.3) and (4.4). By inspection of Eq. (4.4) we see that R cannot be determined without knowing the value for r and without R we cannot use Eq. (4.3) to find V. To proceed we assume a flat rotation curve with fixed $V = 207$ km/s, the average of our previous observations.

Therefore rearranging Eq. (4.3) for R we obtain

$$R = \frac{V R_0 \sin(l)}{V_r + V_0 \sin(l)}, \qquad \text{with} \qquad V = 207 \text{ km/s}. \tag{4.7}$$

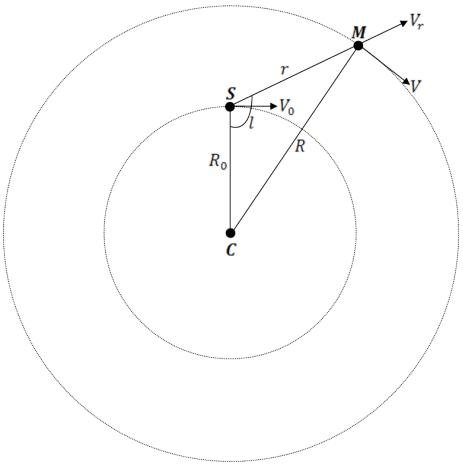

Figure 4.7: The geometry of the Galaxy for a gas cloud observed beyond the solar radius, with all labels defined as in Figure 4.1. Reproduced from Sofue (2013).

We use Eq. 4.7 for observations from Quadrants II and III. Again we plot only for maximum velocity peaks from our observed spectra. Doing this allows us to analyse if our assumption of constant velocity is reasonable.

Plotting these points along with the observed values from inside the solar radius we obtain the rotation curve shown in Figure 4.8. Again these are found using the average of multiple observations for $V_{r,max}$ along each LOS.

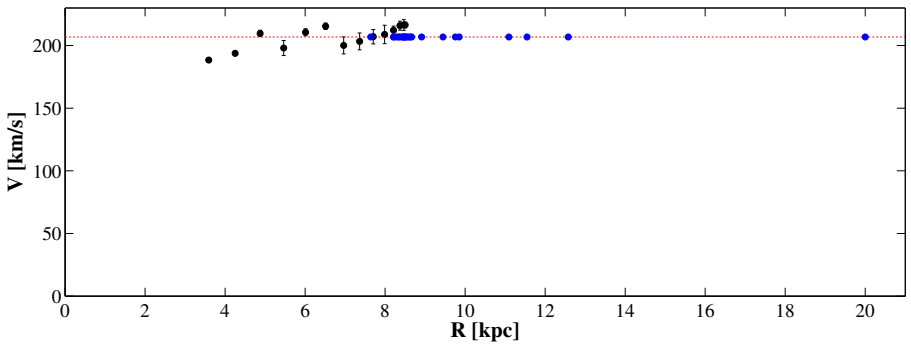

Figure 4.8: Rotation curve with error bars for Quadrant I, black. Projected values for R for constant rotational velocity, blue.

We would expect our projected values for R to be

- greater than 8.5 kpc, since we are looking outside the solar radius,
- not much greater than 15 kpc, since the Galactic radius is of order 10 kpc,
- approximately evenly spaced, since observations were taken at linearly increasing longitudinal values.

We also note that Eq. (4.7) gives $R \to 0$ as $l \to 180°$. Hence for $l \approx 180°$ we obtain innaccurate values for R, removing any points that give unrealistic projections for R we obtain a new, reduced, rotation curve, shown in Figure 4.9.

The points for $R > R_0$ have been forced to lie on the line $V = 207$ km/s. We therefore cannot weight their positions heavily in analysis compared to those for Quadrant I. This is detailed in Section 5.4.1.

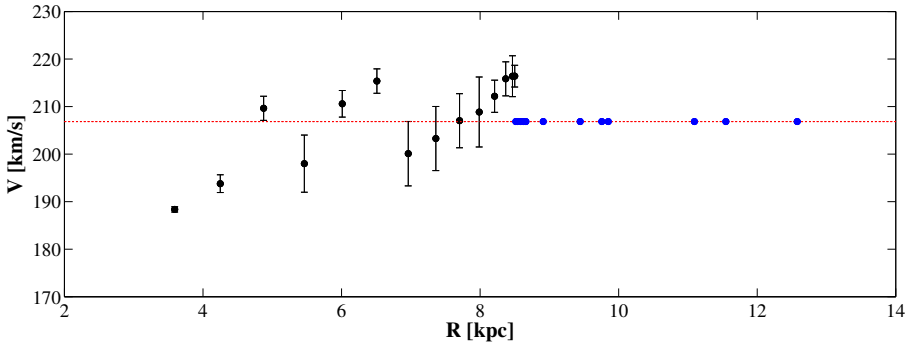

Figure 4.9: Reduced rotation curve for only realistic observations. Inside solar radius observations shown in black, beyond solar radius observations shown in blue.

4.4 Discussion

Throughout this analysis assumptions have been made in order to construct the rotation curve,

- for $R < R_0$ it was assumed that $V_{r,max}$ came from a cloud at the tangential point. This gave the distance R, hence analysis could only be done for one peak per spectrum giving a fixed R for each l,
- for $R > R_0$ it was assumed that all observations had constant rotational velocity, thus allowing derivation of each clouds Galactic radius. This could be applied to all observed Gaussians from each spectrum however results give less information as there can be no variation in rotational velocity. Note that we checked this assumption was reasonable by only using $V_{r,max}$ peaks.

It would be possible to use data from all observed Gaussians if the distance r was known, enabling use of Eq. (4.4) to find R and hence Eq. (4.3) to find V. The distance r can be measured directly by trigonometric (parallax) method or by measurements of the star's luminosity, discussed by Sofue (2013). It is not possible for these measurements to be made using SALSA. In order to construct a full rotation curve for the whole Galactic plane, observations such as these would be necessary.

Chapter 5

Models of Mass Distribution

In this section we discuss different models for how the mass is distributed throughout the Milky Way. Using the forms for given mass distributions, or their gravitational potentials, a rotation curve for the distribution can be derived by use of Eq. (2.4). The form of the rotation curve is fitted, using non-linear modelling in Matlab, to observed data points giving the best estimates for any unknown parameters in the model.

We fit non-linear models using the data points shown in Figure 4.6, with appropriate weightings given to each observation using the size of the confidence intervals shown in Figure 4.5, weightings are given by the reciprocal of the interval width. This is done in order to minimise the distance between the data points and the line given by the model.

5.1 The Bulge Model

The simplest model of the mass distribution is that the gravitating mass is contained within a central sphere at the Galactic centre, hence the mass of the observed clouds is assumed to be negligible in comparison. This allows us to assume that the rotation of the clouds is affected only by the central mass.

Since we are assuming the observed cloud to be outside the Galactic centre we can use Newton's second theorem to model all mass in the central bulge as a point mass and hence directly apply Eq. (2.4), which gives

$$V_b(R) = \sqrt{\frac{GM_b}{R}}, \tag{5.1}$$

where

- $V_b(R)$ is the rotational velocity due to the bulge,
- R is the distance from the Galactic centre, and
- M_b is the mass of the bulge.

5.1.1 Fitting to Data

Applying Eq. (5.1) as the required form of the rotation curve we use our observations to estimate the value of the unknown parameter M_b which gives a rotation curve of the best possible fit to our points. We have measured V in km/s and R in kpc, and for comparative purposes we seek the value of M_b to be measured in solar masses ($M_\odot$). Therefore we must use a value for G that

makes Eq. (5.1) dimensionally consistent.

Taking Eq. (5.1) dimensionally, with our required dimensions, we obtain

$$\text{km}^2 \times \text{s}^{-2} = [\text{G}] \times \text{M}_\odot \times \text{kpc}^{-1}$$

therefore we require

$$[\text{G}] = \text{km}^2 \ \text{s}^{-2} \ \text{M}_\odot^{-1} \ \text{kpc}.$$

We have

$$\begin{aligned} & G = 6.67 \times 10^{-11} \ \text{m}^3 \ \text{kg}^{-1} \ \text{s}^{-2} \\ \Rightarrow \quad & G = 6.67 \times 10^{-11} \ (0.001\text{km})^2 \ (3.24 \times 10^{-20}\text{kpc}) \ (5.03 \times 10^{-31}\text{M}_\odot)^{-1} \ \text{s}^{-2} \\ \Rightarrow \quad & G = 4.30 \times 10^{-6} \ \text{km}^2 \ \text{s}^{-2} \ \text{M}_\odot^{-1} \ \text{kpc}. \end{aligned} \tag{5.2}$$

Applying the form of Eq. (5.1), with the value for G from Eq. (5.2), as a non-linear model for our observed points we obtain the rotation curve shown in Figure 5.1. This is given by

$$V_b(R) = \sqrt{\frac{GM_b}{R}}, \quad \text{with} \quad M_b = 4.19 \times 10^{10} \ \text{M}_\odot.$$

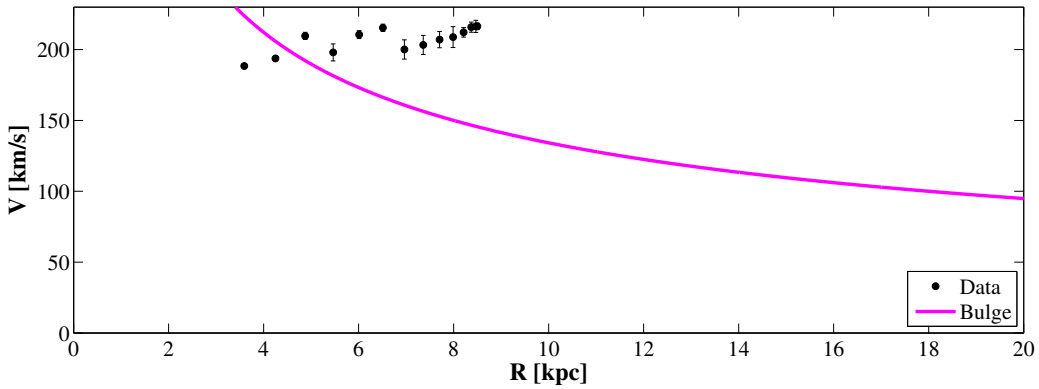

Figure 5.1: Rotation curve for bulge model overlaid on observed points for inside the solar radius.

The estimate for M_b is of the same order of magnitude as the equivalent estimate given by Sofue (2013) of $M_b = 1.80 \times 10^{10} \ \text{M}_\odot$.

Despite giving a reasonable estimate for M_b we can see in Figure 5.1 that the curve does not give a very close fit to our data points. The curve also does not show the constant rotational velocity that we believe the Galaxy to have; the velocity drops off rapidly as we increase the distance from the Galactic centre, this is called Keplerian drop off. We therefore conclude that all mass is not contained only in a central bulge.

5.2 The Exponential Disc Model

We know that most of the stars in the Galaxy lie in a Galactic disc, therefore we assume a disc-like distribution for the mass. Kalberla and Dedes (2008) show that the distribution of HI in an exponential disc gives a reasonable fit to properties observed in the Milky Way for increasing values of R. This is shown in Figure 5.2.

In both plots in Figure 5.2 we see an exponential fit follows closely the observations for large R. We note that it would not have been possible to reproduce these plots with our observed data as we have no observations for larger values of R.

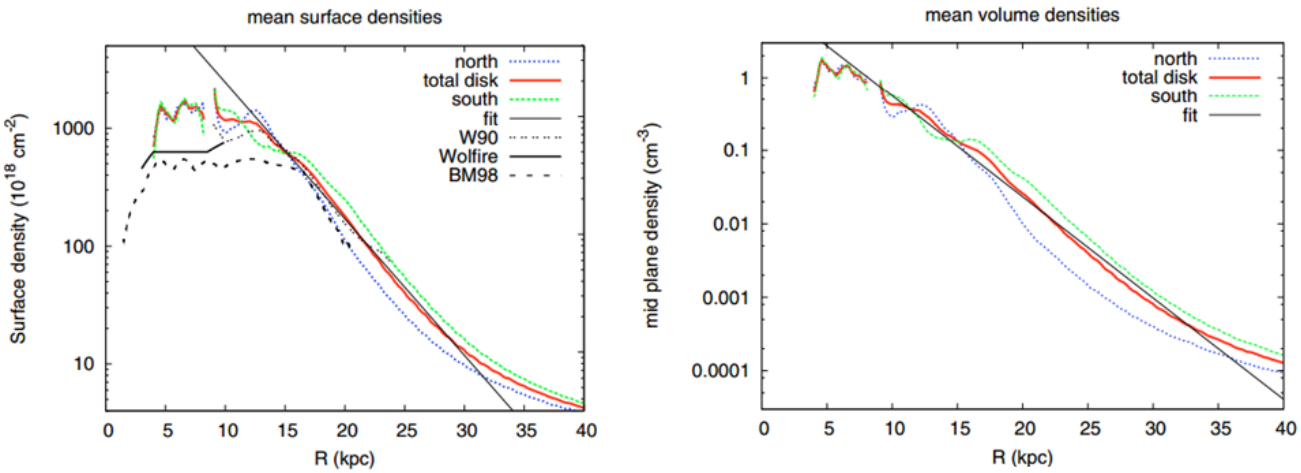

Figure 5.2: Left: Derived mean surface densities of the HI gas perpendicular to the disc (red). Dotted blue and green lines show observations from the northern and southern part of the Milky Way Respectively. Other lines show observations published by others. The straight black lines shows an exponential fit to the observations. Right: Derived average mid-plane volume density of the HI gas (red). Dotted blue and green lines show average volume density for the northern and southern parts of the Milk Way respectively. The straight black lines shows an exponential fit to the observations. (Kalberla and Dedes, 2008, Fig. 3 and 5.)

5.2.1 Derivation

Here we seek the gravitational potential for an exponential disc in order to apply Eq. (2.4). We follow the steps given by Binney and Tremaine (1987). We start with finding a gravitational potential which satisfies Laplace's equation, Eq. (2.6). Since we are assuming an axis-symmetric disc Φ has no dependence on ϕ, it follows that $\Phi = \Phi(R, z)$, and Laplace's equation becomes

$$\frac{1}{R} \cdot \frac{\partial}{\partial R}\left(R\frac{\partial \Phi}{\partial R}\right) + \frac{\partial^2 \Phi}{\partial z^2} = 0.$$

Choosing

$$\Phi(R, z) = J(R) \cdot Z(z),$$

by separation of variables, we obtain

$$\frac{1}{J(R)} \cdot \frac{1}{R} \cdot \frac{d}{dR}\left(R\frac{dJ}{dR}\right) = -\frac{1}{Z} \cdot \frac{d^2 Z}{dz^2} = -k^2,$$

where k is an arbitrary real or complex number. Hence we have

$$\frac{d^2 Z}{dz^2} - k^2 Z = 0, \tag{5.3}$$

$$\frac{1}{R}\frac{d}{dR}\left(R\frac{dJ}{dR}\right) + k^2 J = 0. \tag{5.4}$$

We integrate Eq. (5.3) immediately to obtain

$$Z(z) = S\exp(\pm kz), \tag{5.5}$$

where S is an arbitrary constant. In order to solve Eq. (5.4) we simplify using the substitution $u = kR$. Once simplified we obtain

$$\frac{1}{u}\frac{d}{du}\left(u\frac{dJ}{du}\right) + J(u) = 0. \tag{5.6}$$

The solution of interest, to Eq. (5.6), is the one that remains finite at $u = 0$ ($R = 0$). This is written in the form of the cylindrical Bessel function of order zero, $J_0(u) = J_0(kR)$ and hence gives solutions to Laplace's equation

$$\Phi_{\pm}(R, z) = \exp(\pm kz) J_0(kR). \tag{5.7}$$

We require Laplace's equation to be satisfied for all $z \neq 0$, this is outside the disc where the mass is contained , and Poisson's equation, Eq. (2.5), to be satisfied when $z = 0$, since there is mass contained in the disc.

We now consider the function

$$\Phi_k(R, z) = \exp(-k|z|) J_0(kR), \tag{5.8}$$

where k is real and positive. We note $\Phi_k \to 0$ when $|z| \to \infty$ and also $\Phi_k \to 0$ as $R \to \infty$ since $J_0(u) \to 0$ as $u \to \infty$. Therefore Φ_k satisfies all conditions for it to be the potential generated by an isolated density distribution. Furthermore, for $z > 0$, Φ_k coincides with Φ_-, and for $z < 0$, Φ_k coincides with Φ_+, both given in Eq. (5.7). Therefore Φ_k satisfies Laplace everywhere except in the plane $z = 0$, therefore the gradient of Φ_k suffers a discontinuity at $z = 0$. Binney and Tremaine (1987) show that

$$\Sigma_k(R) = -\frac{k}{2\pi G} J_0(kR), \tag{5.9}$$

where Σ_k is the surface density that generates the discontinuity.

We now use Eqs. (5.8) and (5.9) to find the potential generated by a disc of arbitrary surface density $\Sigma(R)$. If we find a function $S(k)$ such that

$$\Sigma(R) = \int_0^\infty S(k)\Sigma_k(R)\ dk = -\frac{1}{2\pi G}\int_0^\infty S(k) J_0(kR) k\ dk \tag{5.10}$$

then we have

$$\Phi(R, z) = \int_0^\infty S(k)\Phi_k(R, z)\ dk = \int_0^\infty S(k) J_0(kR) \exp(-k|z|)\ dk. \tag{5.11}$$

Hankel transforms express any given function $f(R)$ as the sum of an infinite number of Bessel functions of the first kind $J_\nu(kR)$. The Hankel transform is defined as: if

$$g(k) = \int_0^\infty f(R) J_\nu(kR) R\ dR$$

then g is called the Hankel transform of f, and the inverse transform is given by

$$f(R) = \int_0^\infty g(k) J_\nu(kR) k\ dk.$$

Hence Eq. (5.10) states that $S(k)$ is the Hankel transform of $f(R) = -2\pi G\Sigma$. Therefore we obtain

$$S(k) = -2\pi G \int_0^\infty J_0(kR)\Sigma(R) R\ dR. \tag{5.12}$$

For an exponential disc we set $\Sigma(R) = \Sigma_d \exp(-R/R_d)$, where Σ_d is the surface mass density of the disc and R_d is the scale radius of the disc. Therefore, from Eq. (5.12), we obtain $S(k)$ for an exponential disc. This is given by

$$S(k) = -\frac{2\pi G \Sigma_d R_d^2}{\left[1 + (kR_d)^2\right]^{\frac{3}{2}}} \tag{5.13}$$

where the integral was calculated with help of formula 6.623.2 of Gradshteyn and Ryzhik (1965). We then obtain the potential by substituting Eq. (5.13) into Eq. (5.11), giving

$$\Phi(R, z) = -2\pi G \Sigma_d R_d^2 \int_0^\infty \frac{J_0(kR) \exp(-k|z|)}{\left[1 + (kR_d)^2\right]^{\frac{3}{2}}}\, dk. \tag{5.14}$$

Setting $z = 0$ in Eq. (5.14), for the Galactic plane and using formula 6.552.1 of Gradshteyn and Ryzhik (1965) and formula 9.6.27 of Abramowitz and Stegun (2012) we obtain the potential

$$\Phi(R, 0) = -\pi G \Sigma_d R \left[I_0\left(\frac{R}{2R_d}\right) K_1\left(\frac{R}{2R_d}\right) - I_1\left(\frac{R}{2R_d}\right) K_0\left(\frac{R}{2R_d}\right)\right], \tag{5.15}$$

where I_n and K_n are modified Bessel functions. Differentiating Eq. (5.15) with respect to R and substituting into Eq. (2.4) we obtain the rotational velocity for an exponential disc, shown by Freeman (1970) to be

$$V_d(R)^2 = \pi G \Sigma_d \frac{R^2}{R_d} \left[I_0\left(\frac{R}{2R_d}\right) K_0\left(\frac{R}{2R_d}\right) - I_1\left(\frac{R}{2R_d}\right) K_1\left(\frac{R}{2R_d}\right)\right]. \tag{5.16}$$

5.2.2 Fitting to Data

We now use Eq. (5.16) as the form of the rotation curve in order to estimate the two unknown parameters, the scale radius, R_d, and the surface mass density, Σ_d, using the data to fit a non-linear model. We will seek R_d to be measured in kpc and Σ_d to be measured in $\mathrm{M}_\odot\mathrm{kpc}^{-2}$. This gives the following dimensional version of Eq. (5.16)

$$\left(\frac{\mathrm{km}}{\mathrm{s}}\right)^2 = [G] \times \mathrm{M}_\odot\mathrm{kpc}^{-2} \times \mathrm{kpc}^2 \times \mathrm{kpc}^{-1} \quad \Rightarrow \quad [G] = \mathrm{km}^2\ \mathrm{s}^{-2}\ \mathrm{M}_\odot^{-1}\ \mathrm{kpc}.$$

Therefore we use the same value for the gravitational constant here as we did for the bulge model, specified in Eq. (5.2). The fitted model for Eq. (5.16) is shown in Figure 5.3 and the estimated rotation curve is given by

$$V_d(R) = \sqrt{\pi G \Sigma_d \frac{R^2}{R_d} \left[I_0\left(\frac{R}{2R_d}\right) K_0\left(\frac{R}{2R_d}\right) - I_1\left(\frac{R}{2R_d}\right) K_1\left(\frac{R}{2R_d}\right)\right]},$$

with $R_d = 3.32$ kpc and $\Sigma_d = 1.32 \times 10^8\ \mathrm{M}_\odot\mathrm{kpc}^{-2}$.

We see in Figure 5.3 that the estimated rotation curve follows the observations much more closely than the bulge model. We also note that estimates given by Sofue (2013) for R_d and Σ_d are 3.50 kpc and $8.44 \times 10^8\ \mathrm{M}_\odot\mathrm{kpc}^{-2}$ respectively, which are of equivalent orders of magnitude to our estimates. However, similarly to the bulge model, we observe a Keplerian drop off in rotational velocity as R increases.

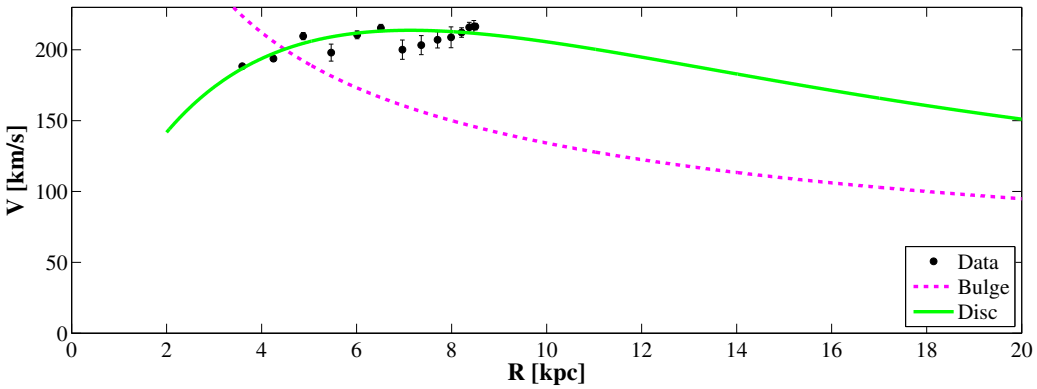

Figure 5.3: Rotation curve for disc model overlaid on observed points for inside the solar radius. Bulge curve also shown for reference.

5.3 The Halo Model

The previously obtained rotation curves do not remain flat as R increases and will always show Keplerian dropoff. In order for a flat rotation curve to be observed the presence of large amounts of unseen matter is widely believed. This dark matter is expected to be in the form of a spherical halo component (Kent, 1986). The extra unseen matter provides gravity allowing the observable matter to orbit at a faster rotational velocity, whilst still remaining in the galaxy, as R increases.

5.3.1 Derivation

The form of a halo density profile, (Kent, 1986), is given by

$$\rho(R) = \frac{\rho_0}{1 + (R/h)^2}, \tag{5.17}$$

where ρ_0 is the central density and h is the core radius. We note that $\rho(R = 0)$ and $\dfrac{d}{dR}\rho(R = 0)$ are both finite making this a desirable density profile.

We use the following to relate the density profile to the mass profile

$$M(R) = \int_V \rho(R)\, dV, \tag{5.18}$$

hence substituting Eq. (5.17) into Eq. (5.18), with appropriate limits for a spherically symmetric halo, we obtain

$$\begin{aligned} M(R) &= \int_0^R \int_0^{2\pi} \int_0^{\pi} \frac{\rho_0}{1 + (R'/h)^2} R'^2 \sin\phi \; d\phi d\theta dR' \\ &= 4\pi\rho_0 h^2 \int_0^R \frac{R'^2}{h^2 + R'^2} \; dR' \\ &= 4\pi\rho_0 h^2 \int_0^R \left(1 - \frac{h^2}{h^2 + R'^2}\right) \; dR' \\ &= 4\pi\rho_0 h^2 R \left[1 - \left(\frac{h}{R}\right) \arctan\left(\frac{R}{h}\right)\right]. \end{aligned} \tag{5.19}$$

Substituting Eq. (5.19) into Eq. (2.4) we have

$$V^2(R) = \frac{GM(R)}{R} = 4\pi G\rho_0 h^2 \left[1 - \left(\frac{h}{R}\right) \arctan\left(\frac{R}{h}\right)\right]. \tag{5.20}$$

As R increases V tends to a constant, giving a flat rotational velocity at $R = \infty$, which we denote V_∞. Therefore we have

$$\lim_{R\to\infty} V(R) = \sqrt{4\pi G\rho_0 h^2} = V_\infty. \tag{5.21}$$

Hence combining Eqs. (5.20) and (5.21) we obtain an equation for the rotational velocity for a mass distribution of a halo, given by

$$V_h(R) = V_\infty \sqrt{1 - \left(\frac{h}{R}\right) \arctan\left(\frac{R}{h}\right)}. \tag{5.22}$$

5.3.2 Fitting to Data

We now use Eq. (5.22) as the required form of rotation curve and the observed points as a means to estimate the value of the unknown parameter h, measured in kpc. Since V_∞ is defined to be the rotational velocity at $R = \infty$ we take this to be 207 km/s. This is the average of our observed points, as we are looking for a constant rotation curve as R increases.

We see that Eq. (5.22) is dimensionally consistent since we are inputting both V_h and V_∞ to be measured in km/s, also that the dimensions of h and R, measured in kpc, immediately cancel out.

Applying the form of Eq. (5.22) as a non-linear model for our observed points we obtain the rotation curve shown in Figure 5.4 and the estimated rotation curve, given by

$$V_h(R) = V_\infty \sqrt{1 - \left(\frac{h}{R}\right) \arctan\left(\frac{R}{h}\right)}, \quad \text{with} \quad V_\infty = 207 \text{ km/s} \quad \text{and} \quad h = -0.22 \text{ kpc}.$$

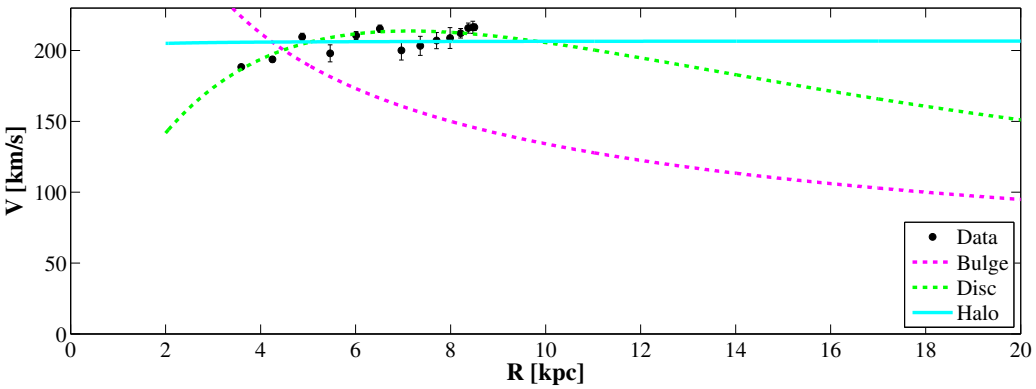

Figure 5.4: Rotation curve for halo model overlaid on observed points for inside the solar radius. Previous model curves also shown for reference.

We can see in Figure 5.4 that the fitted line for the model both follows the points closely and gives the required flat rotation curve. However the value for the radius of the halo, h is clearly unrealistic for a distance. Comparing with the estimated value given by Sofue (2013) which is 12.0 kpc we see this value is more realistic. However it is clear that some contribution from the mass of a halo must be necessary in order to produce a flat rotation curve.

5.4 Combined Model

We now assume that the Galaxy is composed of all three of the components we have, a central bulge, an exponential disc and a dark matter halo. Hence the total rotational velocity is found

by summing the squares of the individual corresponding velocities and modelling them together. This is given by

$$V(R) = \sqrt{V_b(R)^2 + V_d(R)^2 + V_h(R)^2}, \tag{5.23}$$

with the three velocity components as defined respectively in Eqs. (5.1), (5.16) and (5.22). A schematic for the Galactic structure is shown in Figure 5.5.

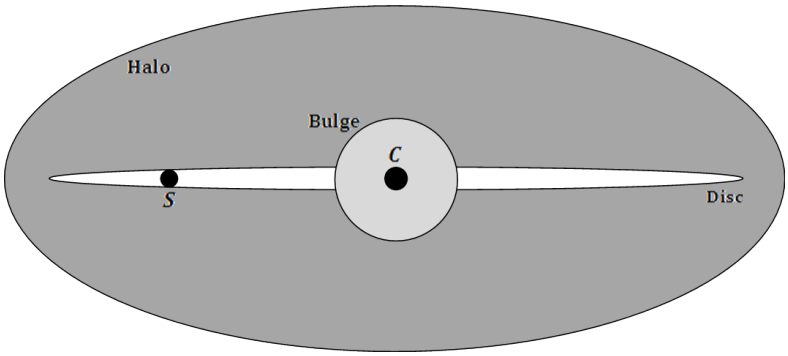

Figure 5.5: Schematic showing three components of the Galaxy. The central Galactic position, C, and the Sun, S, are shown.

5.4.1 Fitting to Data

As previously we use Eq. (5.23) to estimate the unknown parameters based on our observations. Here there are four parameters to be estimated, M_b, Σ_d, R_d, and h. Applying the given equation as a non-linear model we obtain the rotation curve shown in Figure 5.6.

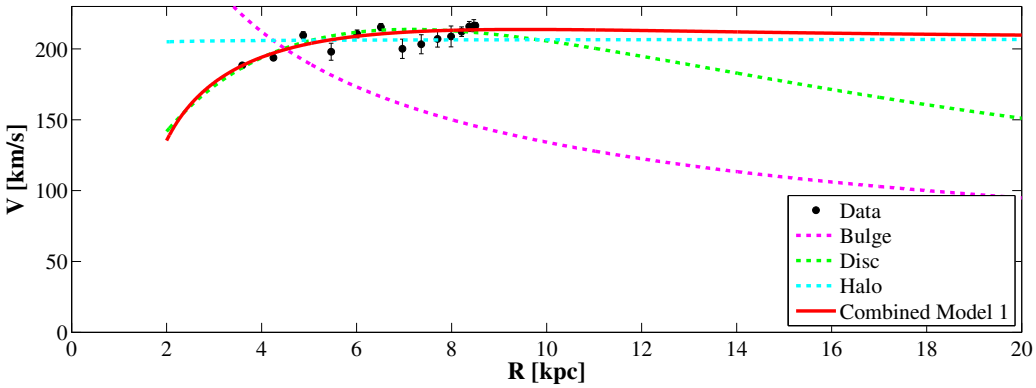

Figure 5.6: Rotation curve for combined model overlaid on observed points for inside the solar radius. Previous curves also shown for reference.

The estimated parameters given by this rotation curve are

$$M_b = -1.42 \times 10^{10}\ \mathrm{M}_\odot, \quad \Sigma_d = 3.94 \times 10^8\ \mathrm{kpc}^{-2}\ M_\odot, \quad R_d = 2.69\ \mathrm{kpc}, \quad h = 0.00\ \mathrm{kpc}.$$

The rotation curve does follow the points well and give a constant rotation curve as R increases. However the estimate for M_b is now showing an unrealistic negative value to give the closest fit.

In order to see the discrepancy between these parameter estimates and Sofue's parameter estimates we plot Sofue's rotation curve compared with our combined curve, this is shown in Figure 5.7.

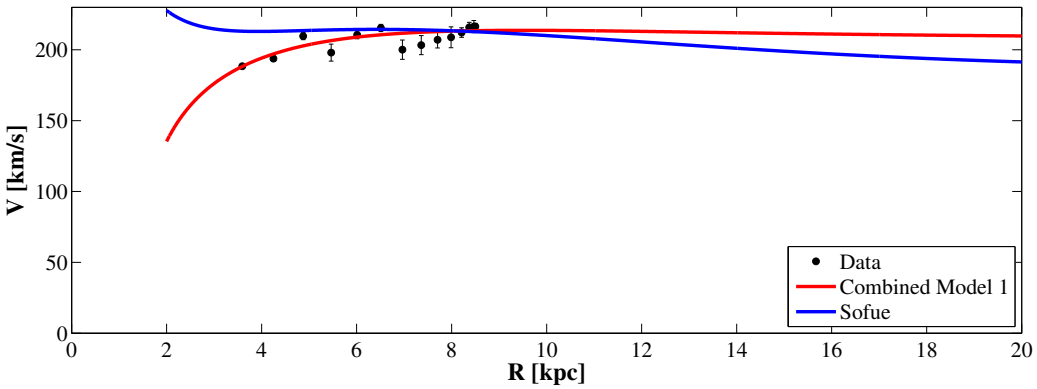

Figure 5.7: Combined model rotation curve compared with rotation curve obtained by Sofue (2013).

In Figure 5.7 we can see our fitted curve begins increasing where Sofue's curve is decreasing. The first two of our observation points are causing the fit to have this form. Hence we conclude that these observations must not have fulfilled the necessary assumptions when the data was transformed as they are not following the rotation found by Sofue. Removing these points and refitting the model gives the rotation curve shown in Figure 5.8.

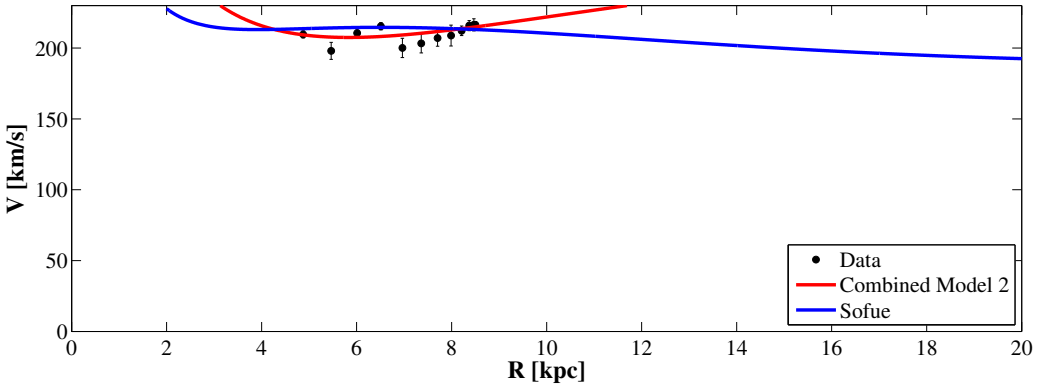

Figure 5.8: Combined model rotation curve, for reduced data, compared with curve by Sofue (2013).

The parameter estimates given by the new model, without the first two data points, are

$$M_b = 3.26 \times 10^{10}\ \mathrm{M}_\odot, \qquad \Sigma_d = 4.27 \times 10^{8}\ \mathrm{kpc}^{-2}\ M_\odot, \qquad R_d = 12.30\ \mathrm{kpc}, \qquad h = 23.87\ \mathrm{kpc}.$$

These estimates are of the same orders of magnitude as Sofue's however our rotation curve does not tend to a constant rotational velocity as we require, seen in Figure 5.8. The curve is shown to increase as R increases beyond the solar radius.

This problem is due to the fact that our observations are limited to within the solar radius. We have no observations to influence our model for larger values of R. We now add to our observations to include the points shown in Figure 4.9 for $R > R_0$. These extra points, beyond the solar radius, are weighted to be of equal weight to the smallest weight from the points from Quadrant I. This prevents these new observations overwhelming the data from Quadrant I but gives them some significance in the model.

The Final Model

Fitting a new non-linear model through all the points, using Eq. (5.23), we obtain the rotation curve shown in Figure 5.9. This new curve closely follows Sofue's for all values of R. A comparison of parameter estimates for the final model, and all previous models, is shown in Table 5.1.

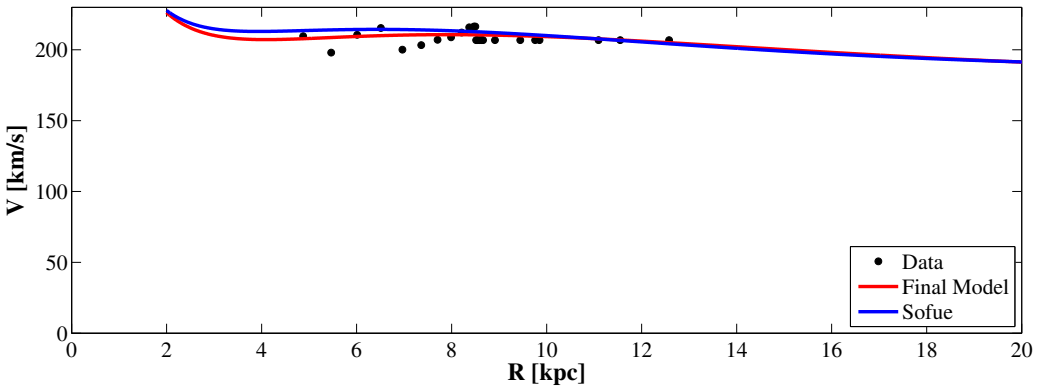

Figure 5.9: Combined model rotation curve for reduced data inside the solar radius, including projected observations for $R > R_0$, compared with rotation curve obtained by Sofue (2013). Error bars for Quadrant I points are omitted.

		Parameter			
		M_b ($M_\odot$)	Σ_d ($M_\odot kpc^{-2}$)	R_d (kpc)	h (kpc)
Model	Bulge	4.19×10^{10}	-	-	-
	Disc	-	1.32×10^{9}	3.32	-
	Halo	-	-	-	-0.22
	Combined 1	-1.42×10^{10}	3.94×10^{8}	2.69	0.00
	Combined 2	3.26×10^{10}	4.27×10^{8}	12.30	23.87
	Final	1.86×10^{10}	7.22×10^{8}	4.13	15.48
	Sofue	1.80×10^{10}	8.44×10^{8}	3.50	12.00

Table 5.1: Summary of all parameter estimates obtained from non-linear modelling using observed data points. Compared with parameter estimates given by Sofue (2013).

From inspection of Table 5.1 and Figures 5.1 - 5.9 we conclude that the "Final Model" shows the best fit to the observations, the closest fit in comparison to Sofue's curve and the closest four estimates for the parameters compared to Sofue's. The "Final Model" is made up of three contributions towards the mass distribution, the bulge, disc and halo. In Figure 5.10 we can see how the three contributions combine to make the final model, these have been plotted for both "Final Model" and Sofue's model for comparison.

The two breakdowns, shown in Figure 5.10, follow a very similar pattern, as we expect given the similarities in parameter estimates. It is also clearly shown how the contributions from the dark matter halo are contributing to a constant rotational velocity for increasing values of R.

The final rotation curve gives a close fit to the data points observed using SALSA, and also matches closely the rotation curve and parameters estimated by Sofue (2013). The fact that these results replicate Sofue's reasonably closely is both impressive and surprising. Our data consisted of observations made only using HI observation with a small radio telescope, SALSA, over a period of less than a month. Contrastingly the data used in Sofue's analysis, shown in Figure 5.11, were collected over at least 31 years using 8 different data collection methods.

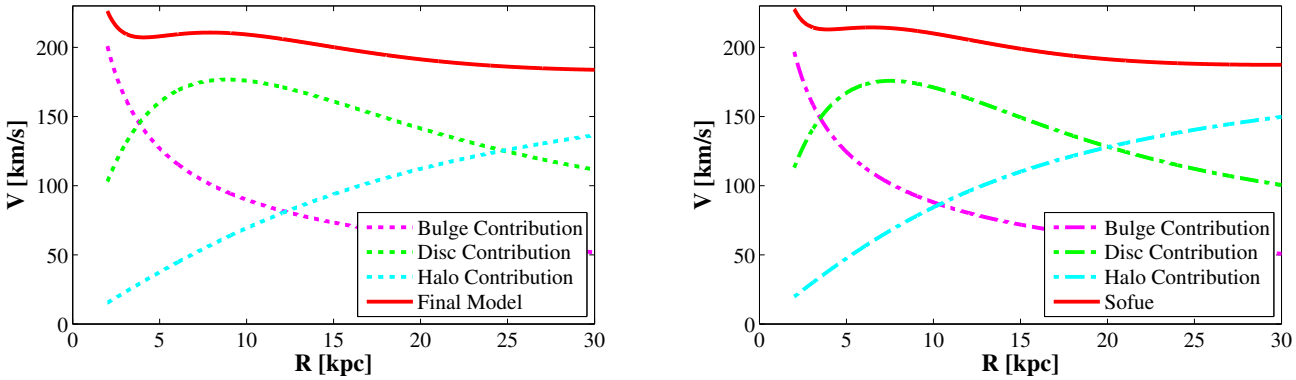

Figure 5.10: Left: Plot showing how my final combination model is made by the sums of the three components based on derived estimates. Right: Equivalent plot showing breakdown of Sofue's rotation curve using his estimates of model parameters.

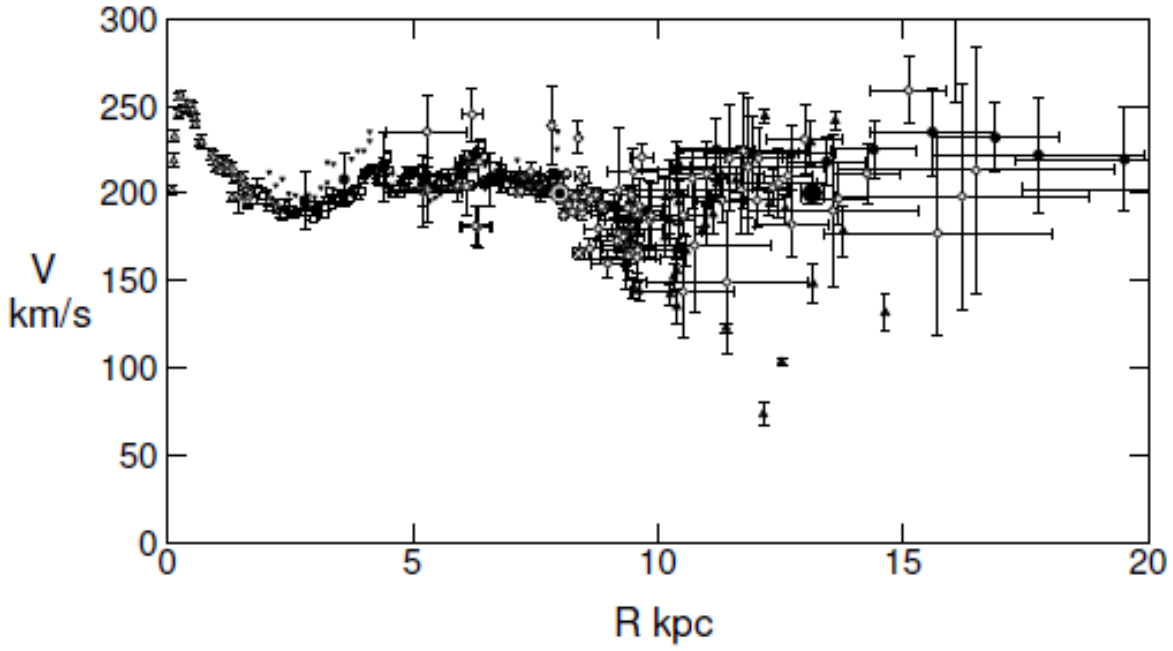

Figure 5.11: Compiled data points from different sources. Details given by Sofue (2013, Fig. 5.).

Chapter 6

HI Gas Distribution in the Milky Way

We now analyse where the observed HI gas lies in the Galactic plane, therefore we continue analysis of only data for $b = 0°$. In our previous analysis we have only used the data from the maximum velocity peaks in our spectra. Now we will take into account all peaks and hence look at all data collected for the Galactic plane. We have confirmed that a good estimate of rotation is to have a constant rotational velocity. Hence for ease of calculation, in this section, we assume a constant rotational velocity of $V = V_0$ and remember that we have observed V_r and l for each HI cloud, seen as spectral peaks.

6.1 Preliminary Calculations

Using known V_r and l, and the assumption of constant rotational velocity we can simplify Eq. (4.3) and rearrange for R in terms of known quantities, obtaining

$$R = \frac{V_0 R_0 \sin(l)}{V_r + V_0 \sin(l)}. \tag{6.1}$$

This can be applied to all observations to find the distance of each observed cloud from the Galactic centre. In order to create a map of the gas position we convert R and l for each of our observations to be r and θ; where r is the distance from us to the observed cloud and θ is the polar angle, shown in Figure 6.1.

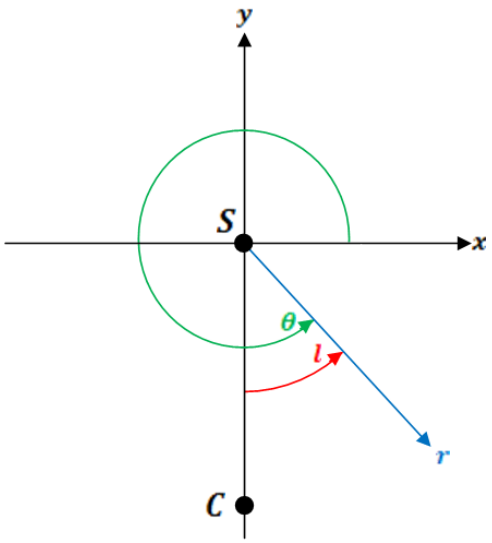

Figure 6.1: Illustration of conversion from Galactic longitude coordinate, l, to polar coordinate θ.

Clearly, by inspection of Figure 6.1 we have

$$\theta = l + 270°. \tag{6.2}$$

From Eq. (4.4) we can rearrange for r, this gives us two possible solutions, $r = r_+$ and $r = r_-$, given by

$$r_\pm = \pm\sqrt{R^2 - R_0^2 \sin^2(l)} + R_0 \cos(l). \tag{6.3}$$

We require that $r > 0$ as it is a distance. Therefore beyond the solar radius ($l > 90°$) there is only one positive solution, r_+, since $\cos(l) < 0$. However within the solar radius there can be two positive solutions. The two possible values for r can be seen in Figure 4.1, these are the point M and the point further away, where our LOS crosses the inner circle a second time. Further analysis is needed to determine which of these values is correct. For our analysis we will use both possible values and highlight where choices can be made.

Finally in order to create the map we must convert our polar coordinates (r, θ), to cartesian coordinates, (x, y) as follows

$$x = r\cos\theta \qquad \text{and} \qquad y = r\sin\theta + R_0, \tag{6.4}$$

we note that the shift for the y coordinate is to place the Galactic centre at the origin.

6.2 Data Analysis

Applying Eqs. (6.1) to (6.4) to all of the V_r we have observed, at specified l values, we obtain a map of the positions of all observed clouds, shown in Figure 6.2.

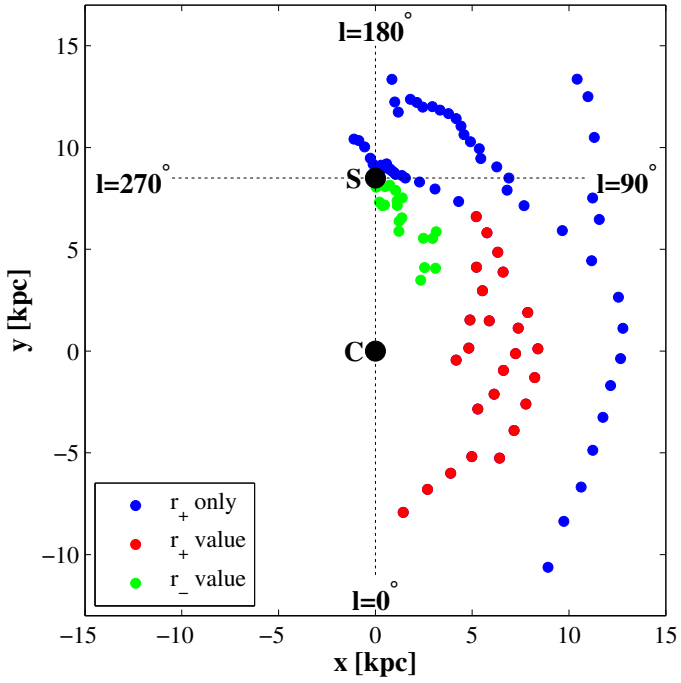

Figure 6.2: Map of the positions of observed HI clouds in the Galactic plane. Blue points are those clouds which only gave a positive solution for r_+. Where both r_+ and r_- values gave a positive solution both sets have been plotted; red for r_+ and green for r_-. Galactic longitude values are shown.

In Figure 6.2 we see a hint of the spiral arm formation in the Galactic plane that was shown in

Figure 1.3. The general shape of two spiral arms is present, possibly the Perseus Arm and the Sagittarius Arm. Where two positive solutions are obtained it is possible to determine which of these values is correct by observing again at the given longitude but at varying latitudes. If the observed cloud is the more distant it is less likely we will continue to observe it at higher Galactic latitude. This further analysis has not been possible as several more observing sessions would have been necessary.

A map of the distribution of neutral hydrogen in the Galactic plane was also given by Burton (1974), shown in Figure 6.3. Here we also see the spiral arm structure of the Milky Way shown by the areas of highest density.

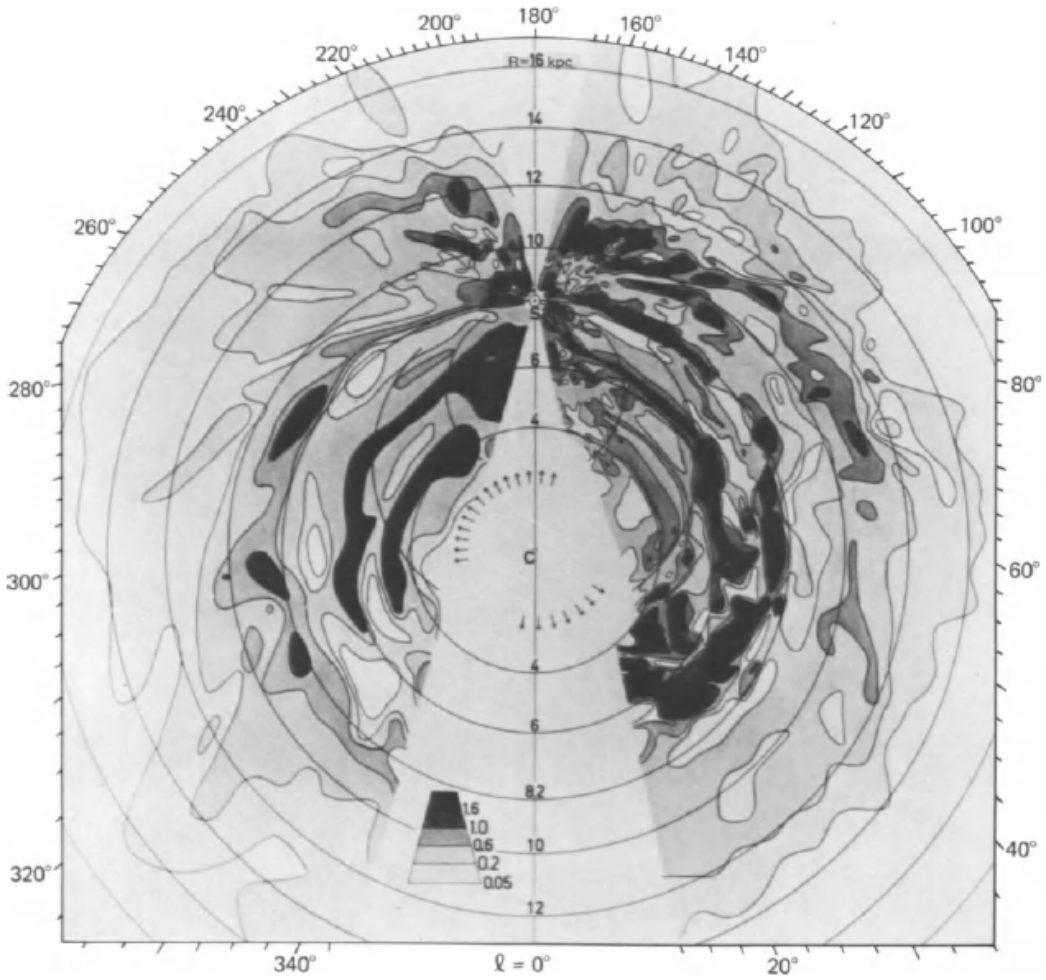

Figure 6.3: Distribution of neutral hydrogen densities determined from Dutch and Austrailian surveys. (Burton, 1974, Fig. 4.9).

The Galactic map, Figure 6.2, has been created based on the assumption of constant rotational velocity throughout the Galactic plane. However the rotation curve, Figure 5.9, does not have constant rotational velocity close to the Galactic centre, approximately $R < 3$ kpc. Therefore some positions may be inaccurate, however since we cannot determine R without knowing V we cannot be certain which these points are.

Chapter 7

Rotational Velocity out of the Galactic Plane

We have, so far, looked only at observations for within the Galactic plane, fixed latitude, $b = 0°$. We now look at observations with varied latitude and fixed longitude. This enables us to analyse how rotational velocity varies related to distance from the Galactic plane.

We make use of the observations for fixed longitude, $l = 80°$ and for varied latitude $-30° \leq b \leq 30°$. The choice of observing at fixed $l = 80°$ was made because observing within the solar radius allows us to apply Eq. (4.6) to obtain the rotational velocity. Again this is done by using only the observed maximum velocity peaks, as in Section 4.2. This longitude was also a suitable choice since we obtained consistently strong spectra at $l = 80°$ and $b = 0°$ hence it is likely spectra obtained out of the plane at 80° will continue to be strong.

We note that

- for $b > |30°|$ spectra become too weak for any peaks to be observed,
- 5 readings were taken on each LOS allowing calculation of averages, standard deviations and confidence intervals, as in Chapter 4,
- we cannot be observing the whole velocity of the cloud on the LOS, assumed by Eq. (4.6), however since we are looking at only a small variation outside the Galactic plane this will give a reasonable approximation for V.

7.1 Distance from Galactic Plane Derivation

Using the line ST from Figure 4.2 we obtain the schematic shown in Figure 7.1, where P is the observed point.

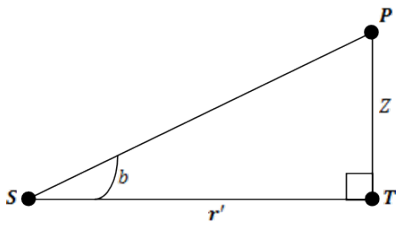

Figure 7.1: Schematic showing the position of a cloud out of the Galactic plane, P. Z is the distance from the plane. S shows the Sun's position and T shows the tangential point from Figure 4.2. r' is the relabeled value r from Figure 4.2 as it is no longer the distance to the cloud.

From Figures 7.1 and 4.2 respectively we have

$$Z = r' \tan(b) \quad \text{and} \quad r' = R_0 \cos(l) \quad \text{which gives} \quad Z = R_0 \cos(l) \tan(b), \tag{7.1}$$

yielding an expression for Z in terms of known quantities.

7.2 Data Analysis

We now apply Eqs. (4.6) and (7.1) to the maximum velocity peaks for each of the observed spectra to find the rotational velocity and Z-distance respectively. We obtain the plot shown in Figure 7.2.

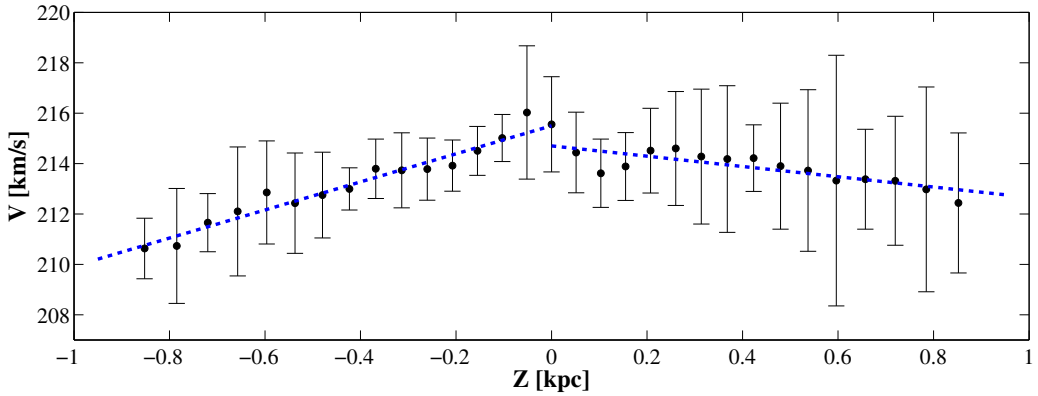

Figure 7.2: Observed points for all $V_{r,max}$ for $l = 80°$ and $-30° \leq b \leq 30°$. Error bars showing the associated 95% confidence intervals are over laid for each point. Dotted blue lines show the linear models fitted to the upper and lower sections using Matlab.

The best fit lines were derived using a linear model in Matlab, using the appropriate standard deviations for the observations to define weightings, as in Chapter 4. The equations for the two lines are given by

$$V = \begin{cases} 215.5 + 5.6Z & \text{for} \quad Z < 0 \\ 214.7 - 2.0Z & \text{for} \quad Z > 0 \end{cases}.$$

This gives a drop off in rotational velocity, ΔV, of 5.6km s^{-1}/kpc for negative Z and 2.0km s^{-1}/kpc for positive Z. The uncertainty in observations for $Z > 0$ is considerably larger than the observations for $Z < 0$, this may be why the magnitude of the drop off in rotational velocity is observed to be less. We would expect the drop off to be the same for both above and below the Galactic plane owing to the assumed symmetry of the Galaxy. We now compare this with results found elsewhere.

Results are based on different scale heights, h_R, for varying R. To calculate this we use the associated formula, given by Kalberla and Kerp (2009),

$$h_R = h_0 \exp\left(\frac{R - R_0}{R_\odot}\right) \quad \text{where} \quad h_0 = 0.15\text{kpc} \quad \text{and} \quad R_\odot = 9.8\text{kpc}.$$

We require the scale height for the associated R where we observe at the tangential point on the LOS with $l = 80°$. Applying Eq. (4.5) we obtain $R = 8.4$ kpc for $l = 80°$. Hence the scale height is

$$h_{8.4} = 0.15 \exp\left(\frac{8.4 - 8.5}{9.8}\right) = 0.11\text{kpc}.$$

Kalberla and Kerp (2009) give $\Delta V = 1.3\text{km s}^{-1}/h_R$. Therefore their estimate for the drop off in rotational velocity is

$$\Delta V = 1.3\text{km s}^{-1}/0.11\text{kpc} = 11.8\text{km s}^{-1}/\text{kpc}.$$

Levine et al. (2008) give $\Delta V = 2.2\text{km s}^{-1}/h_R$. Therefore their estimate for the drop off in rotational velocity is

$$\Delta V = 2.2\text{km s}^{-1}/0.11\text{kpc} = 20.0\text{km s}^{-1}/\text{kpc}.$$

For comparison these estimates have been overlaid with the observed data, shown in Figure 7.3.

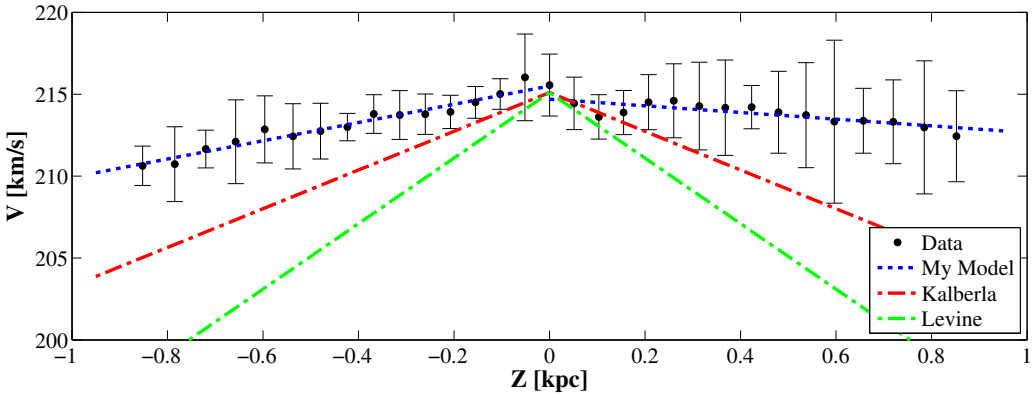

Figure 7.3: Points and confidence intervals equivalent to those shown in Figure 7.2. Red and green lines show drop off predicted by Kalberla and Kerp (2009) and Levine et al. (2008) respectively.

All three predictions show the velocity dropping off as distance from the Galactic plane increases, all with different magnitudes. Disagreement on the magnitude is common and discussed further by Kalberla and Kerp (2009). In order to find ΔV in terms of a scale height more observing sessions at other fixed longitudes would be necessary.

Taking a fixed Galactic latitude and observing for varied Galactic longitudes, would enable us to construct a rotation curve for gas out of the Galactic plane. For example $b = -30°$ gives a rotation curve for $|Z| \simeq 0.8$ kpc A plot of further rotation curves for different $|Z|$ is given by Kalberla and Kerp (2009), shown in Figure 7.4. This reinforces the drop off in rotational velocity as the distance, Z, increases away from the Galactic plane.

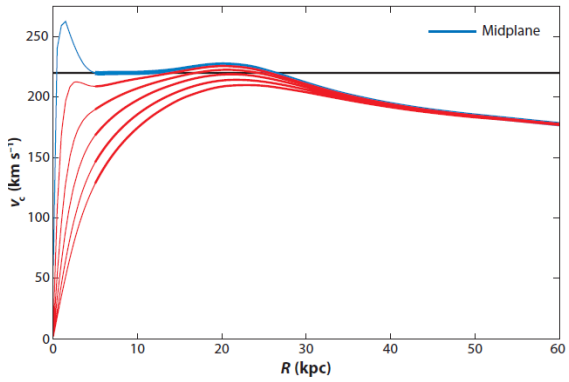

Figure 7.4: The upper blue curve represents the rotation curve in the Galactic plane. The case $V = 220$km/s is plotted for comparison. Other curves (red) show circular velocities for out of the plane, $|Z| = 1$ to 5 kpc. (Kalberla and Kerp, 2009, Fig. 2).

Chapter 8

Turbulent Velocities within HI Clouds

As previously mentioned in Section 3.2, we have observed the standard deviation of each fitted Gaussian giving a measure of the width. The Doppler broadening of a Gaussian profile is caused by the motion of atoms due to the gas temperature and by the random turbulent motion of the gas. Lang (1999) gives that the standard deviation of a Gaussian profile, σ, showing a Doppler Shift is given by

$$2\sigma^2 = \frac{\nu_{mn}^2}{c^2}\left(\frac{2kT_k}{M} + V^2\right), \tag{8.1}$$

where

- ν_{mn} is the frequency of the emitted radiation - for a 21cm wavelength we have $\nu_{mn} = 1.42 \times 10^9$ Hz,
- $c = 2.99 \times 10^5$ km/s - the speed of light,
- $k = 1.38 \times 10^{-29}$ km^2 kg s^{-2} K^{-1} - this is Boltzmann's constant,
- T_k is the kinetic temperature of observed atoms - for cold interstellar hydrogen we have $T_k \simeq 100$K, (Ferriere, 2001).
- M is the mass of a single atom from our observation - for hydrogen atoms we have $M = 1.66 \times 10^{-27}$kg,
- V is the turbulent velocity within the gas cloud, we take this to be measured in km/s.

Taking Eq. (8.1) dimensionally we obtain

$$[\sigma]^2 = \frac{\text{s}^{-2}}{\text{km}^2\text{s}^{-2}}\left(\frac{\text{km}^2\ \text{kg}\ \text{s}^{-2}\ \text{K}^{-1} \times \text{K}}{\text{kg}} + \frac{\text{km}^2}{\text{s}^2}\right) \quad \Rightarrow \quad [\sigma] = \text{s}^{-1},$$

this gives the standard deviation of a Gaussian measured in Hz. However, from SALSA, we observed σ measured in km/s. Taking the observed standard deviation σ_{obs} to be the sum of the turbulent and temperature contributions, we have

$$\sigma_{obs} = \sigma_V + \sigma_T, \tag{8.2}$$

where σ_V is the contribution from the turbulent velocity and σ_T is from the temperature, noting we require these components measured in km/s.

We will hence seek the value of σ_T, in km/s, enabling us to find the turbulent velocity, σ_V of our observed clouds. Starting with Eq. (8.1), we find the width of the Gaussian profile with

no turbulent velocity, $V = 0$, this is σ_T. Relabeling σ, in Eq. (8.1), as $\sigma_{T,Hz}$ in order to identify the temperature component measured in Hz, we have

$$\sigma^2_{T,Hz} = \frac{\nu^2_{mn} k T_k}{c^2 M}, \quad \Rightarrow \quad \sigma_{T,Hz} = 4.33 \times 10^3 \text{ Hz}. \tag{8.3}$$

Also using a result from Lang (1999) we relate observations of frequency, ν, to the corresponding velocity, V, given by

$$\nu = \nu_{mn}\left(1 - \frac{V}{c}\right) \quad \Rightarrow \quad \sigma_{T,Hz} = \nu_{mn}\left(1 - \frac{V_{\min}}{c}\right) - \nu_{mn}\left(1 - \frac{V_{\max}}{c}\right) = \frac{\nu_{mn}}{c}\left(V_{\max} - V_{\min}\right),$$

which gives

$$\sigma_{T,Hz} = \frac{\nu_{mn}}{c}\sigma_{T,km/s}, \tag{8.4}$$

where $\sigma_{T,km/s}$ is the standard deviation of the Gaussian profile, measured in km/s. Substituting from Eq. (8.3) into Eq. (8.4) we obtain

$$\sigma_{T,km/s} = 0.91\text{km/s}.$$

Therefore from Eq. (8.2) we have

$$\sigma_V = \sigma_{obs} - 0.91. \tag{8.5}$$

This tells us that 0.91 km/s of the standard deviation from each observed Gaussian is movement of the gas particles due to their temperature. Hence if there were no turbulence a much sharper Gaussian peak would be observed. Therefore the remainder of the Gaussian width is due to the presence of turbulent velocities within the cloud.

Applying Eq. (8.5) to all observed values of σ we obtain the plots in Figure 8.1 showing the turbulent velocity, V_t, of each observed cloud. We are assuming all observed gas clouds to be the same 'cold' temperature, $T_k = 100$K.

For observations taken in the Galactic plane, Figure 8.1: [1], [2] and [3], there is a reasonably constant relationship between V_t and position in the plane. For observations out of the Galactic plane, Figure 8.1: [4], a constant turbulent velocity is clearly observed as distance from the Galactic plane is increased for both positive and negative values of Z. Both in and out of the plane we observe the constant turbulent velocity, $V_t \simeq 10$ km/s. We hence conclude that turbulent velocity is approximately constant throughout the Galaxy. Taking averages of all observations for V_t we find constant turbulent velocity $V_t = 13.8 \pm 3.5$km/s, where the confidence interval is the average of all individual 95% confidence intervals for all observations. Agertz et al. (2009) quotes $V_t \sim 10$km/s as a general result for disc galaxies, which is in agreement with our observations.

It is given by Ferriere (2001) that 21cm emission is observed in both cold (T_k=50K$-$100K) and warm (T_k=6000$-$10000K) neutral hydrogen. For each temperature we observe a different turbulent velocity. The range of values are shown in Table 8.1. Assuming a higher temperature for the gas gives a correspondingly lower value for turbulent velocities. However for a large range in temperature, 50$-$10000K, there is a comparatively tiny change in turbulent velocity. We cannot deduce the T_k of the HI gas therefore it is possible that V_t is lower than that shown in Figure 8.1 for some observed clouds.

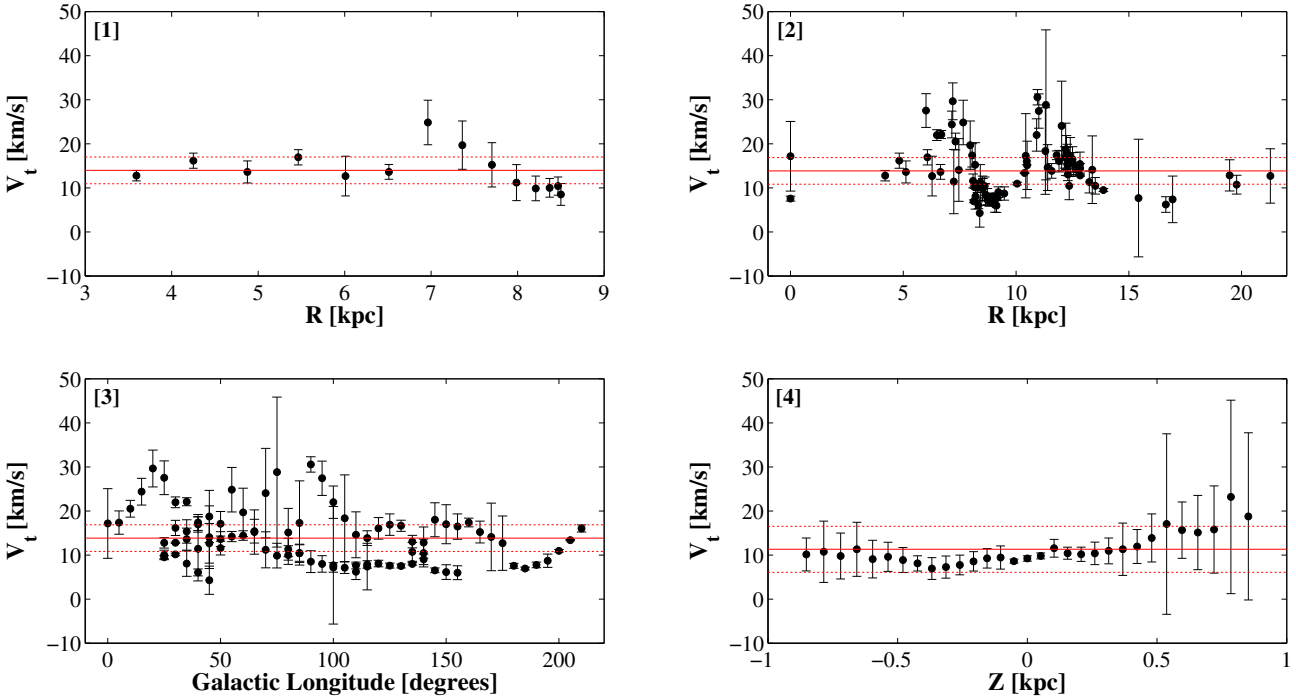

Figure 8.1: Plots showing turbulent velocities of particles in observed HI clouds. Overlaid on each plot is the average of plotted V_t values and 95% confidence interval from the average width of the 95% error bars shown. [1] shows V_t for clouds plotted in Figure 4.6 for Quadrant I. [2] shows V_t for all observed clouds in the Galactic plane with R found by Eq. (6.1). [3] shows V_t for the same observations as [2] plotted by Galactic longitude made by the LOS. [4] show V_t for clouds plotted in Figure 7.2 for varying latitudes.

T_k [K]	σ_T [km/s]	V_t [km/s]
50	0.64	14.12
100	0.91	13.84
6000	7.06	7.69
10000	9.12	5.64

Table 8.1: Table showing the width of a Gaussian, σ_T, for a specified temperature, T_k and the turbulent velocity V_t we observe for that temperature.

Chapter 9

Summary

Neutral hydrogen was traced in the Milky Way by observing the 21cm emission line using a radio telescope, 'SALSA'. For each observation multiple peaks are seen showing the 21cm emission corresponding to hydrogen gas clouds. To these peaks Gaussian curves are fitted, using these we infer properties about the observation: the intensity of the signal and the radial velocity and standard deviation of each cloud. Noting that the position of each cloud is known in Galactic coordinates, (l, b).

For observations made in the Galactic plane, $b = 0°$, a rotation curve is constructed, using known radial velocity and Galactic longitude to find rotational velocity and distance from the Galactic centre. This rotation curve is constructed separately for observations inside and beyond the solar radius based on different assumptions. The obtained rotation curve is shown in Figure 4.9. From this we concluded an approximately constant rotational velocity as distance from the Galactic centre increases, given by $V(R) = 207 \pm 4$ km/s.

Non-linear modelling is used to fit the forms of various mass models to the observed points allowing us to understand the mass distribution in the Milky Way. Through comparison of a rotation curve given by Sofue (2013) we concluded the total Galactic mass to be comprised of mass given by a central bulge, an exponential disc and a dark matter halo; parameters of interest are given in Table 5.1. The combined masses of these three components give an approximately flat rotation curve as R increases, shown in Figure 5.10. This shows the existence of dark matter to be a reasonable explanation in explaining the difference between the expected Keplarian rotation curve and the approximately flat observed curve.

Assuming a constant rotational velocity throughout the Milky Way allows us to plot the positions of each observed cloud in the Galactic plane given we know it's radial velocity and Galactic longitude. A map of the locations of all observed clouds is shown in Figure 6.2. We see hydrogen lying in spiral arms in the Galactic plane, as shown in Figure 1.3. It is not possible to create a full map of the Galaxy using 'SALSA' owing to it's global location.

Analysing observations for $-30° \leq b \leq 30°$, allows examination of how rotational velocity varies with distance from the Galactic plane. A drop off in rotational velocity is observed, this is largest for $b < 0°$, however results for $b > 0°$ are more uncertain. For $b < 0°$ we have $\Delta V = 5.6\text{km s}^{-1}/\text{kpc}$. We would expect results for both above and below the Galactic plane to be in agreement, as quoted in other results. The magnitude of the drop off does not show agreement with other results, with Kalberla and Kerp (2009) and Levine et al. (2008) both predicting a faster drop off, shown in Figure 7.3. However all results agree that rotational velocity decreases as distance from the Galactic plane increases.

The standard deviation of each observed Gaussian gives a measure of the width of the peak. The broadening of the Gaussian profile is caused by the motion of atoms due to the gas temperature and by the random turbulent motion of the gas. We find an approximately constant turbulent velocity for all gas clouds in the Milky Way. For gas of temperature 100K the turbulent velocity is, $V_t = 13.84$ km/s. As the temperature of the gas increases a larger contribution of the width comes from the temperature and hence a smaller contribution from turbulence, for our fixed observed widths.

Further observing sessions would allow us to determine the true location of the uncertain HI clouds in the Galactic map, Figure 6.2. Also more observing sessions at varied Galactic latitudes would enable construction of rotation curves for out of the Galactic plane, such as those shown in Figure 7.4. Finally observing again six months after the original observations would allow us to observe more of the sky, and hence allow construction of a more detailed rotation curve and a fuller Milky Way map.

Appendix A

VARYING LONGITUDE		Observation Date/Time [yy-mm-dd: tttt]											
b [°]	*l* [°]	13-10-09: 1200	13-10-09: 1500	13-10-11: 0700	13-10-13: 1200	13-10-14: 1600	13-10-15: 0700	13-10-15: 1900	13-10-15: 2300	13-10-16: 1600	13-10-21: 1900	13-10-22: 2000	TOTAL OBS
0	0	1	1			1							**3**
0	5	1	1			1							**3**
0	10	1	1			1							**3**
0	5	1	1			1							**3**
0	20	1	1			1							**3**
0	25	1	1			1				1			**4**
0	30	1	1			1				1			**4**
0	35	1	1		1	1				1			**5**
0	40	1	1		1	1				1			**5**
0	45	1	1		1	1		1					**5**
0	50	1	1		1	1		1					**5**
0	55	1	1		1	1		1					**5**
0	60	1	1		1	1		1					**5**
0	65	1	1		1	1		1					**5**
0	70	1	1	1	1	1							**5**
0	80	1	1	1	1	1							**5**
0	85	1	1	1	1	1							**5**
0	90	1	1	1	1	1							**5**
0	95	1	1	1	1	1							**5**
0	100	1	1	1	1	1							**5**
0	105	1	1	1	1	1							**5**
0	110	1	1	1	1	1							**5**
0	115	1	1	1	1	1							**5**
0	120	1	1	1	1	1							**5**
0	125	1	1	1	1	1							**5**
0	130	1	1	1	1	1							**5**
0	135	1	1	1	1	1							**5**
0	140	1	1	1	1	1							**5**
0	145	1	1	1	1	1							**5**
0	150	1	1	1	1	1							**5**
0	155	1	1	1	1	1							**5**
0	160	1	1	1	1	1							**5**
0	165	1	1	1	1	1							**5**
0	170	1	1	1	1	1							**5**
0	175	1		1	1	1	1						**5**
0	180			1			1	1	1		1		**5**
0	185			1			1	1	1		1		**5**
0	190			1			1	1	1			1	**5**
0	195			1			1	1	1			1	**5**
0	200			1			1		1				**3**
0	205			1			1		1				**3**
0	210			1			1		1				**3**

VARYING LATITUDE		Observation Date/Time [yy-mm-dd: tttt]						
b [°]	*l* [°]	13-11-08: 1100	13-11-09: 2000	13-12-26: 1400	14-01-03: 1100	14-01-29: 1600	14-01-31: 1200	TOTAL OBS
-30	80	1	1	1	1	1		**5**
-28	80	1	1	1	1	1		**5**
-26	80	1	1	1	1	1		**5**
-24	80	1	1	1	1	1		**5**
-22	80	1	1	1	1	1		**5**
-20	80	1	1	1	1	1		**5**
-18	80	1	1	1	1	1		**5**
-16	80	1	1	1	1	1		**5**
-14	80	1	1	1	1	1		**5**
-12	80	1	1	1	1	1		**5**
-10	80	1	1	1	1	1		**5**
-8	80	1	1	1	1	1		**5**
-6	80	1	1	1	1	1		**5**
-4	80	1	1	1	1	1		**5**
-2	80	1	1	1	1	1		**5**
0	80	1	1	1	1	1		**5**
2	80	1	1	1	1	1		**5**
4	80	1	1	1	1	1		**5**
6	80	1	1	1	1	1		**5**
8	80	1	1	1	1	1		**5**
10	80	1	1	1	1	1		**5**
12	80	1	1	1	1	1		**5**
14	80	1	1	1	1	1		**5**
16	80	1	1	1	1	1		**5**
18	80	1	1	1	1	1		**5**
20	80	1	1	1	1	1		**5**
22	80	1	1	1	1	1		**5**
24	80	1		1	1	1	1	**5**
26	80	1		1	1	1	1	**5**
28	80	1		1	1	1	1	**5**
30	80	1		1	1	1	1	**5**

Above are the dates and times of all observations taken using SALSA in order to collect data for analysis.

Appendix B

			Antenna Temperature [K]							Velocity [km/s]							Standard Deviation [km/s]						
b [°]	l [°]	Gaussian #	1	2	3	4	5	Mean	S.D.	1	2	3	4	5	Mean	S.D.	1	2	3	4	5	Mean	S.D.
0	**0**	**1**	10.4	36.4	36.2			**27.7**	**15.0**	-4.1	-2.1	-2.3			**-2.8**	**1.1**	22.7	15.2	16.3			**18.1**	**4.0**
0	**5**	**1**	18.5	59.5	53.5			**43.8**	**22.1**	1.5	0.7	1.0			**1.1**	**0.4**	19.8	17.6	17.4			**18.3**	**1.3**
0	**10**	**1**	30.1	56.5	59.7			**48.7**	**16.2**	7.8	5.2	5.6			**6.2**	**1.4**	22.5	21.0	20.8			**21.4**	**1.0**
0	**15**	**1**	32.5	61.7	64.1			**52.7**	**17.6**	11.2	10.6	10.5			**10.7**	**0.4**	27.1	24.3	24.5			**25.3**	**1.5**
0	**20**	**1**	12.3	46.7	53.5			**37.5**	**22.1**	11.9	14.8	14.3			**13.7**	**1.6**	28.1	32.0	31.5			**30.5**	**2.1**
0	**25**	**1**	10.5	17.8	18.4	20.4		**16.8**	**4.3**	95.6	95.1	95.7	95.3		**95.4**	**0.3**	12.9	13.8	13.7	14.4		**13.7**	**0.6**
0	**25**	**2**	19.2	33.3	36.9	40.9		**32.6**	**9.4**	43.3	39.5	35.7	35.7		**38.5**	**3.6**	25.8	28.5	30.4	29.1		**28.5**	**1.9**
0	**25**	**3**	25.7	42.6	38.2	41.3		**36.9**	**7.7**	2.4	2.2	2.5	2.1		**2.3**	**0.2**	11.7	10.6	10.5	11.0		**10.9**	**0.5**
0	**25**	**4**	11.2	17.4	17.5	20.7		**16.7**	**4.0**	-34.7	-36.0	-36.6	-36.7		**-36.0**	**1.0**	10.4	10.2	10.5	10.6		**10.4**	**0.2**
0	**30**	**1**	21.1	28.9	29.4	32.5		**28.0**	**4.8**	84.7	83.8	82.5	84.2		**83.8**	**1.0**	15.9	17.1	18.0	17.3		**17.1**	**0.9**
0	**30**	**2**	26.6	33.9	36.9	41.5		**34.7**	**6.2**	37.9	34.2	31.3	33.1		**34.1**	**2.8**	22.6	22.8	22.4	23.8		**22.9**	**0.6**
0	**30**	**3**	38.3	44.9	41.6	46.7		**42.9**	**3.7**	4.7	4.9	4.4	4.5		**4.6**	**0.2**	10.9	11.1	11.1	11.2		**11.1**	**0.1**
0	**30**	**4**	15.0	19.2	21.5	24.7		**20.1**	**4.1**	-36.4	-37.7	-36.9	-37.7		**-37.2**	**0.6**	13.7	13.6	13.8	13.6		**13.7**	**0.1**
0	**35**	**1**	16.6	19.7	22.3	24.0	23.7	**21.2**	**3.1**	82.7	82.4	85.6	83.0	83.6	**83.5**	**1.3**	13.5	14.4	16.6	14.7	13.5	**14.5**	**1.3**
0	**35**	**2**	45.5	45.0	35.0	52.6	55.1	**46.6**	**7.8**	34.8	34.7	33.0	33.8	34.8	**34.2**	**0.8**	23.7	23.0	22.4	22.8	23.2	**23.0**	**0.5**
0	**35**	**3**	40.5	39.9	43.5	44.9	43.6	**42.5**	**2.2**	3.8	4.5	5.7	4.6	4.6	**4.6**	**0.7**	7.7	8.5	11.5	8.5	8.7	**9.0**	**1.5**
0	**35**	**4**	16.0	17.2	21.2	19.6	22.1	**19.2**	**2.6**	-42.0	-40.1	-40.6	-40.6	-40.6	**-40.8**	**0.7**	17.1	16.5	14.0	16.4	17.4	**16.3**	**1.4**
0	**40**	**1**	42.1	49.8	25.0	47.8	48.8	**42.7**	**10.4**	55.5	54.9	62.0	56.1	54.5	**56.6**	**3.1**	16.3	18.1	18.1	18.1	18.6	**17.8**	**0.9**
0	**40**	**2**	50.4	52.1	56.6	54.5	50.3	**52.8**	**2.7**	23.7	24.2	26.5	24.2	24.4	**24.6**	**1.1**	11.6	10.4	18.9	11.0	9.8	**12.3**	**3.7**
0	**40**	**3**	47.9	59.1	37.3	55.3	56.3	**51.2**	**8.8**	2.3	3.0	3.4	2.5	3.1	**2.9**	**0.4**	6.4	6.9	7.0	7.0	7.5	**7.0**	**0.4**
0	**40**	**4**	19.8	23.5	21.2	24.8	24.3	**22.7**	**2.1**	-42.0	-42.8	-44.7	-42.9	-43.8	**-43.2**	**1.1**	17.9	19.6	17.3	17.8	18.9	**18.3**	**0.9**
0	**45**	**1**	51.5	45.4	44.0	50.2	49.4	**48.1**	**3.3**	52.8	54.7	56.3	56.2	55.2	**55.0**	**1.4**	12.9	11.9	14.5	11.4	17.1	**13.6**	**2.3**
0	**45**	**2**	52.7	51.4	56.7	61.7	50.6	**54.6**	**4.6**	16.5	20.2	24.8	21.1	25.4	**21.6**	**3.7**	16.0	18.1	11.9	18.4	10.4	**15.0**	**3.6**
0	**45**	**3**	26.9	29.8	49.3	32.7	50.5	**37.9**	**11.2**	1.0	1.5	2.7	1.2	3.6	**2.0**	**1.1**	3.7	4.0	6.7	4.3	7.2	**5.2**	**1.6**
0	**45**	**4**	19.8	21.1	25.5	26.3	26.2	**23.8**	**3.1**	-49.6	-49.0	-44.8	-48.9	-43.5	**-47.2**	**2.8**	18.3	17.9	20.3	17.2	24.6	**19.7**	**3.0**
0	**50**	**1**	57.5	59.9	56.9	69.9	75.0	**63.8**	**8.1**	45.6	45.9	48.1	46.2	48.4	**46.8**	**1.3**	14.2	13.7	14.7	14.0	15.9	**14.5**	**0.9**
0	**50**	**2**	61.4	64.0	61.6	72.4	77.5	**67.4**	**7.2**	7.6	7.8	9.4	7.8	9.4	**8.4**	**0.9**	11.8	11.8	13.4	12.2	13.3	**12.5**	**0.8**
0	**50**	**3**	19.3	20.7	23.7	24.5	33.1	**24.3**	**5.4**	-51.1	-51.8	-52.4	-52.5	-51.0	**-51.8**	**0.7**	19.9	16.9	16.6	19.0	17.6	**18.0**	**1.4**
0	**55**	**1**	54.9	63.4	62.8	62.2	61.5	**60.9**	**3.5**	16.6	17.5	22.8	18.2	24.3	**19.9**	**3.5**	23.2	23.9	27.9	24.7	29.1	**25.8**	**2.6**
0	**55**	**2**	17.4	20.6	24.5	21.3	23.7	**21.5**	**2.8**	-60.5	-60.3	-57.6	-60.7	-57.5	**-59.3**	**1.6**	15.3	14.7	14.3	15.4	15.7	**15.1**	**0.6**
0	**60**	**1**	71.1	71.5	51.4	79.6	81.7	**71.1**	**12.0**	10.3	10.1	17.6	10.6	15.2	**12.8**	**3.4**	17.9	18.7	24.4	19.3	22.6	**20.6**	**2.8**
0	**60**	**2**	21.8	23.3	20.0	27.8	33.1	**25.2**	**5.3**	-65.8	-66.9	-60.5	-65.5	-63.2	**-64.4**	**2.5**	14.8	15.2	16.2	14.9	15.5	**15.3**	**0.6**
0	**65**	**1**	80.2	86.8	59.9	91.6	76.9	**79.1**	**12.1**	5.3	5.5	11.7	6.1	9.7	**7.6**	**2.9**	14.0	14.1	19.1	14.8	18.8	**16.1**	**2.6**
0	**65**	**2**	21.2	26.4	24.8	28.5	29.9	**26.2**	**3.4**	-67.2	-68.5	-66.2	-68.1	-66.7	**-67.3**	**1.0**	17.7	14.3	17.4	16.1	16.0	**16.3**	**1.4**
0	**70**	**1**	91.5	99.0	20.7	65.4	100.0	**75.3**	**33.6**	1.9	1.8	-2.8	7.8	1.8	**2.1**	**3.8**	10.9	11.0	11.2	15.8	11.5	**12.1**	**2.1**
0	**70**	**2**	20.1	22.1	4.8	26.7	24.3	**19.6**	**8.7**	-57.6	-59.4	-56.9	-68.1	-60.7	**-60.5**	**4.5**	29.0	27.7	25.4	16.0	26.7	**25.0**	**5.2**
0	**75**	**1**	86.3	98.6	44.6	86.2	96.1	**82.4**	**21.9**	-0.3	-0.6	-2.2	2.5	-1.0	**-0.3**	**1.7**	9.8	10.2	9.9	13.2	10.8	**10.8**	**1.4**
0	**75**	**2**	22.1	25.1	11.5	34.7	26.5	**24.0**	**8.4**	-45.5	-49.8	-48.1	-67.7	-53.6	**-53.0**	**8.8**	35.9	33.4	33.2	14.4	31.7	**29.7**	**8.7**
0	**80**	**1**	93.5	96.2	38.0	77.4	101.3	**81.3**	**25.8**	-0.9	-0.9	-2.9	2.1	-1.5	**-0.8**	**1.8**	11.0	11.6	11.4	9.0	11.5	**10.9**	**1.1**
0	**80**	**2**	25.3	27.8	11.9	31.3	30.9	**25.4**	**7.9**	-41.2	-41.3	-42.4	-38.1	-42.6	**-41.1**	**1.8**	16.8	14.5	13.9	20.6	14.3	**16.0**	**2.8**
0	**80**	**3**	19.5	22.3	10.7	32.7	26.1	**22.3**	**8.1**	-79.3	-78.2	-79.0	-72.5	-79.2	**-77.6**	**2.9**	11.4	13.6	10.5	13.2	12.3	**12.2**	**1.3**
0	**85**	**1**	59.4	69.7	53.6	102.9	77.7	**72.7**	**19.3**	-1.8	-2.8	-4.4	0.3	-5.2	**-2.8**	**2.2**	9.9	10.9	12.1	11.0	12.6	**11.3**	**1.1**
0	**85**	**2**	31.4	32.0	24.0	29.4	37.5	**30.8**	**4.9**	-34.6	-41.8	-44.6	-35.9	-45.6	**-40.5**	**5.0**	24.6	21.9	14.6	16.7	13.1	**18.2**	**4.9**
0	**85**	**3**	21.2	23.3	19.5	30.0	31.7	**25.1**	**5.4**	-82.8	-83.4	-81.5	-77.0	-81.6	**-81.3**	**2.5**	10.9	10.5	11.1	13.0	11.3	**11.4**	**1.0**
0	**90**	**1**	54.7	61.9	50.0	72.4	56.3	**59.1**	**8.6**	-3.9	-4.2	-4.8	-1.8	-3.2	**-3.6**	**1.2**	8.8	8.8	10.1	11.3	8.1	**9.4**	**1.3**
0	**90**	**2**	31.0	36.0	27.4	29.7	31.9	**31.2**	**3.2**	-47.7	-49.5	-51.2	-53.5	-43.8	**-49.2**	**3.7**	32.2	31.8	31.3	30.0	32.1	**31.5**	**0.9**
0	**95**	**1**	55.1	59.7	52.3	59.9	60.0	**57.4**	**3.5**	-6.1	-6.1	-6.2	-3.3	-6.9	**-5.7**	**1.4**	8.2	8.5	8.5	10.6	8.7	**8.9**	**1.0**
0	**95**	**2**	39.8	42.2	34.5	32.4	42.5	**38.3**	**4.6**	-47.8	-49.1	-49.2	-52.5	-51.1	**-49.9**	**1.9**	27.9	27.4	26.9	31.8	27.7	**28.3**	**2.0**
0	**100**	**1**	53.8	55.5	54.5	62.3	57.0	**56.6**	**3.4**	-6.8	-6.3	-6.6	-4.2	-6.6	**-6.1**	**1.1**	8.1	7.4	7.9	8.9	8.1	**8.1**	**0.6**
0	**100**	**2**	37.5	39.2	36.7	32.7	40.9	**37.4**	**3.1**	-50.8	-49.7	-49.4	-38.7	-50.9	**-47.9**	**5.2**	22.9	23.2	24.8	19.8	23.8	**22.9**	**1.9**
0	**100**	**3**	6.2	5.5	6.6	18.5	7.7	**8.9**	**5.4**	-103.3	-104.7	-103.1	-73.3	-102.2	**-97.3**	**13.4**	5.3	6.3	5.7	20.7	4.8	**8.6**	**6.8**
0	**105**	**1**	64.8	64.5	63.1	47.9	65.5	**61.1**	**7.5**	-8.6	-8.7	-8.0	-4.1	-8.6	**-7.6**	**2.0**	8.1	8.4	8.3	6.9	8.5	**8.0**	**0.7**
0	**105**	**2**	45.6	50.1	45.0	36.1	47.2	**44.8**	**5.3**	-54.7	-55.1	-54.0	-44.1	-55.1	**-52.6**	**4.8**	17.0	16.3	17.4	28.2	17.5	**19.3**	**5.0**
0	**110**	**1**	72.1	65.6	72.6	57.8	71.9	**68.0**	**6.4**	-9.7	-9.7	-9.2	-4.5	-9.9	**-8.6**	**2.3**	8.6	8.7	8.7	7.9	8.8	**8.5**	**0.4**
0	**110**	**2**	56.3	52.7	56.7	39.7	58.6	**52.8**	**7.7**	-53.5	-53.6	-53.2	-48.7	-53.8	**-52.6**	**2.2**	14.2	14.4	14.2	20.3	14.5	**15.5**	**2.7**
0	**110**	**3**	11.1	10.6	12.1	6.3	13.7	**10.8**	**2.8**	-100.2	-101.6	-101.2	-101.2	-101.3	**-101.1**	**0.5**	8.0	7.3	7.3	5.6	7.4	**7.1**	**0.9**
0	**115**	**1**	65.7	61.4	64.6	61.7	66.0	**63.9**	**2.2**	-10.0	-10.1	-9.7	-6.6	-10.0	**-9.3**	**1.5**	9.0	9.0	9.1	8.1	8.6	**8.8**	**0.4**
0	**115**	**2**	53.6	49.7	49.9	49.6	53.2	**51.2**	**2.0**	-53.8	-54.8	-53.1	-49.4	-53.8	**-53.0**	**2.1**	14.9	15.3	15.3	13.3	15.0	**14.7**	**0.8**
0	**115**	**3**	13.1	12.2	12.3	6.3	12.6	**11.3**	**2.8**	-100.8	-100.6	-100.6	-93.4	-101.3	**-99.3**	**3.3**	7.1	6.8	7.3	13.1	7.1	**8.3**	**2.7**
0	**120**	**1**	62.1	59.8	59.0	60.4	66.0	**61.5**	**2.8**	-10.9	-10.8	-10.2	-7.3	-11.1	**-10.1**	**1.6**	9.2	8.9	9.4	8.4	9.1	**9.0**	**0.4**
0	**120**	**2**	45.8	44.7	45.5	46.3	50.5	**46.5**	**2.3**	-55.5	-56.6	-55.2	-48.9	-56.1	**-54.5**	**3.2**	16.5	17.9	18.4	15.2	16.9	**17.0**	**1.3**

			Antenna Temperature [K]							Velocity [km/s]							Standard Deviation [km/s]						
b [°]	*l* [°]	Gaussian #	1	2	3	4	5	Mean	S.D.	1	2	3	4	5	Mean	S.D.	1	2	3	4	5	Mean	S.D.
0	**125**	**2**	47.4	47.2	51.7	37.6	50.5	**46.9**	**5.5**	-55.2	-55.4	-56.7	-48.7	-55.2	**-54.2**	**3.1**	18.3	17.7	19.4	16.0	17.7	**17.8**	**1.2**
0	**130**	**1**	57.8	56.0	55.0	58.8	63.7	**58.3**	**3.4**	-9.9	-9.8	-9.6	-9.1	-10.0	**-9.7**	**0.4**	8.6	8.3	8.5	8.1	8.6	**8.4**	**0.2**
0	**130**	**2**	55.1	53.0	47.8	34.8	63.2	**50.8**	**10.5**	-52.3	-51.9	-52.1	-49.7	-52.4	**-51.7**	**1.1**	17.1	18.2	17.9	17.9	16.6	**17.6**	**0.6**
0	**135**	**1**	71.3	63.3	71.1	66.0	60.5	**66.4**	**4.8**	-9.9	-10.4	-10.0	-9.7	-9.9	**-10.0**	**0.2**	8.8	9.1	9.0	8.8	8.9	**8.9**	**0.1**
0	**135**	**2**	67.9	61.5	65.2	48.5	59.7	**60.5**	**7.4**	-47.1	-46.8	-48.9	-50.5	-46.8	**-48.0**	**1.6**	13.9	13.0	14.7	14.6	13.6	**14.0**	**0.7**
0	**135**	**3**	13.9	14.3	16.3	8.3	13.0	**13.1**	**3.0**	-88.0	-83.4	-89.2	-96.4	-86.6	**-88.7**	**4.8**	12.2	12.7	10.7	10.2	12.3	**11.6**	**1.1**
0	**140**	**1**	72.5	62.9	69.2	62.8	64.7	**66.4**	**4.3**	-10.9	-11.6	-11.7	-9.1	-11.3	**-10.9**	**1.1**	9.9	10.3	10.5	8.9	10.1	**9.9**	**0.6**
0	**140**	**2**	76.2	64.3	67.5	43.4	66.4	**63.5**	**12.2**	-42.9	-42.9	-44.9	-46.6	-43.4	**-44.2**	**1.6**	11.2	10.1	10.7	14.2	10.8	**11.4**	**1.6**
0	**140**	**3**	16.7	15.6	18.4	7.7	14.0	**14.5**	**4.1**	-78.5	-72.3	-79.4	-91.1	-77.2	**-79.7**	**6.9**	14.6	15.9	14.1	11.2	12.9	**13.7**	**1.8**
0	**145**	**1**	49.1	52.8	45.9	48.9	52.2	**49.8**	**2.8**	-6.7	-7.5	-7.4	-6.8	-6.9	**-7.1**	**0.4**	7.0	7.5	7.6	7.7	7.4	**7.4**	**0.3**
0	**145**	**2**	63.5	61.7	59.8	42.2	65.3	**58.5**	**9.3**	-37.4	-40.0	-39.0	-37.9	-38.2	**-38.5**	**1.0**	18.5	17.7	22.4	18.4	17.6	**18.9**	**2.0**
0	**150**	**1**	46.8	57.6	57.1	31.2	47.5	**48.0**	**10.7**	-7.0	-7.8	-7.0	-4.8	-7.2	**-6.8**	**1.1**	6.8	7.6	7.7	5.7	7.4	**7.1**	**0.9**
0	**150**	**2**	72.3	71.0	75.7	51.4	69.4	**67.9**	**9.6**	-34.2	-36.7	-37.8	-29.7	-34.7	**-34.6**	**3.1**	18.1	14.8	19.0	20.7	16.9	**17.9**	**2.3**
0	**155**	**1**	39.0	50.0	45.2	31.7	37.3	**40.6**	**7.1**	-5.8	-6.2	-6.3	-8.1	-5.8	**-6.4**	**1.0**	6.3	7.2	6.6	8.2	6.2	**6.9**	**0.8**
0	**155**	**2**	67.3	66.6	72.2	56.1	68.9	**66.2**	**6.0**	-29.4	-31.5	-31.2	-28.1	-28.7	**-29.8**	**1.5**	17.0	15.2	18.6	18.8	17.3	**17.4**	**1.5**
0	**160**	**1**	57.1	55.4	81.6	49.6	67.6	**62.3**	**12.6**	-20.8	-21.5	-21.6	-20.6	-20.6	**-21.0**	**0.5**	17.8	18.2	18.7	18.9	17.8	**18.3**	**0.5**
0	**165**	**1**	58.4	29.1	89.3	40.2	64.3	**56.3**	**23.2**	-16.8	-17.4	-17.8	-18.7	-16.9	**-17.5**	**0.8**	15.5	15.1	16.1	18.3	15.7	**16.1**	**1.3**
0	**170**	**1**	48.2	6.3	103.6	23.1	54.9	**47.2**	**37.1**	-13.3	-12.3	-13.9	-16.8	-13.4	**-13.9**	**1.7**	12.2	21.8	13.3	14.9	12.8	**15.0**	**3.9**
0	**175**	**1**	21.8	108.3	10.0	10.6	114.0	**52.9**	**53.4**	-10.5	-10.0	-16.3	-11.0	-9.8	**-11.5**	**2.7**	11.3	12.0	19.1	13.3	12.4	**13.6**	**3.1**
0	**180**	**1**	98.0	102.5	97.6	104.7	66.6	**93.9**	**15.5**	-5.1	-4.6	-2.0	-4.5	-5.0	**-4.3**	**1.3**	8.7	8.7	8.0	8.5	8.5	**8.5**	**0.3**
0	**185**	**1**	84.9	96.9	76.6	104.4	32.3	**79.0**	**28.2**	-1.2	-0.6	1.2	-0.5	-3.3	**-0.9**	**1.6**	7.9	7.6	8.0	7.8	8.0	**7.9**	**0.2**
0	**190**	**1**	79.5	94.6	30.5	102.6	74.0	**76.2**	**28.0**	2.3	2.5	3.5	3.1	2.7	**2.8**	**0.5**	8.8	8.4	9.2	8.6	8.5	**8.7**	**0.3**
0	**195**	**1**	68.2	71.5	5.7	83.1	34.6	**52.6**	**31.8**	6.3	6.8	3.7	7.3	5.3	**5.9**	**1.4**	10.4	9.9	8.5	10.1	9.3	**9.6**	**0.8**
0	**200**	**1**	64.6	68.0	64.4			**65.7**	**2.0**	11.1	11.6	12.1			**11.6**	**0.5**	11.9	11.7	12.0			**11.9**	**0.1**
0	**205**	**1**	54.6	44.4	48.4			**49.1**	**5.1**	16.8	16.6	17.0			**16.8**	**0.2**	14.3	14.2	14.4			**14.3**	**0.1**
0	**210**	**1**	41.8	52.1	31.0			**41.6**	**10.6**	20.3	20.7	21.2			**20.7**	**0.5**	16.6	16.8	17.4			**16.9**	**0.4**

Above are details of all the data extracted from spectra for observations made in the Galactic plane.

Appendix C

			Antenna Temperature [K]							Velocity [km/s]							Standard Deviation [km/s]						
b [°]	*l* [°]	Gaussian #	1	2	3	4	5	Mean	S.D.	1	2	3	4	5	Mean	S.D.	1	2	3	4	5	Mean	S.D.
-30	**80**	**1**	12.5	17.8	16.9	15.9	17.1	**16.0**	**2.1**	-6.3	-6.9	-5.5	-6.0	-5.4	**-6.0**	**0.6**	13.5	13.3	12.1	12.2	8.7	**12.0**	**1.9**
-28	**80**	**1**	14.1	18.5	16.3	16.8	20.1	**17.1**	**2.3**	-5.4	-7.5	-6.8	-5.3	-4.7	**-5.9**	**1.2**	12.8	17.4	13.7	11.2	7.7	**12.6**	**3.5**
-26	**80**	**1**	15.4	17.9	18.4	18.2	22.7	**18.5**	**2.6**	-4.6	-6.0	-4.8	-5.1	-4.5	**-5.0**	**0.6**	11.8	14.7	10.7	13.1	7.7	**11.6**	**2.7**
-24	**80**	**1**	17.4	17.6	16.5	19.9	26.1	**19.5**	**3.9**	-3.6	-6.8	-4.4	-3.5	-4.4	**-4.6**	**1.3**	11.4	18.6	13.0	11.5	11.1	**13.1**	**3.1**
-22	**80**	**1**	16.2	17.1	21.4	19.1	23.4	**19.4**	**3.0**	-4.1	-5.4	-2.7	-3.4	-3.4	**-3.8**	**1.0**	11.9	14.0	8.7	10.8	9.1	**10.9**	**2.2**
-20	**80**	**1**	16.9	18.5	20.2	20.7	24.6	**20.2**	**2.9**	-5.1	-5.5	-3.4	-3.5	-3.6	**-4.2**	**1.0**	13.0	13.5	9.9	10.3	10.4	**11.4**	**1.7**
-18	**80**	**1**	19.8	22.6	27.7	22.3	28.2	**24.1**	**3.7**	-4.9	-4.2	-2.6	-3.7	-4.2	**-3.9**	**0.9**	12.6	10.8	8.6	10.4	11.1	**10.7**	**1.4**
-16	**80**	**1**	26.3	28.7	34.3	27.6	33.7	**30.1**	**3.6**	-3.8	-4.0	-2.9	-3.7	-3.9	**-3.7**	**0.4**	10.0	10.8	8.4	10.2	10.2	**9.9**	**0.9**
-14	**80**	**1**	32.4	38.0	39.6	29.8	39.9	**35.9**	**4.6**	-2.9	-3.3	-2.8	-1.9	-3.4	**-2.9**	**0.6**	9.0	10.1	8.7	6.7	9.2	**8.8**	**1.3**
-12	**80**	**1**	37.5	39.2	42.4	35.4	42.2	**39.3**	**3.0**	-2.8	-3.4	-2.9	-1.8	-3.8	**-2.9**	**0.8**	8.8	10.7	9.2	7.2	9.6	**9.1**	**1.3**
-10	**80**	**1**	36.6	43.8	46.9	41.7	47.8	**43.3**	**4.5**	-3.0	-3.1	-2.7	-2.0	-3.7	**-2.9**	**0.6**	10.0	10.4	9.7	7.6	10.2	**9.6**	**1.1**
-8	**80**	**1**	40.6	49.4	50.4	47.2	57.0	**48.9**	**5.9**	-3.0	-3.0	-2.8	-1.8	-3.1	**-2.7**	**0.5**	10.6	11.5	10.7	8.5	10.6	**10.4**	**1.1**
-6	**80**	**1**	48.2	67.5	62.2	60.2	74.4	**62.5**	**9.7**	-2.4	-2.0	-2.3	-1.4	-2.7	**-2.2**	**0.5**	11.9	11.8	11.3	9.1	11.4	**11.1**	**1.1**
-4	**80**	**1**	60.8	86.3	78.8	74.5	89.1	**77.9**	**11.2**	-2.0	-1.9	-1.6	-0.8	-1.8	**-1.6**	**0.5**	12.6	12.5	11.5	10.0	9.7	**11.3**	**1.3**
-2	**80**	**1**	76.2	104.6	97.8	93.2	107.4	**95.9**	**12.3**	-0.2	0.6	-0.5	-0.1	-2.9	**-0.6**	**1.3**	10.6	10.6	10.1	10.3	10.7	**10.4**	**0.2**
-2	**80**	**2**	17.7	26.3	18.8	18.2	26.2	**21.4**	**4.4**	-45.7	-48.9	-46.3	-43.5	-54.7	**-47.8**	**4.3**	32.7	32.4	35.2	34.3	32.5	**33.4**	**1.2**
0	**80**	**1**	92.7	116.1	106.3	103.3	116.6	**107.0**	**9.9**	-0.5	-1.1	-1.3	0.0	-2.6	**-1.1**	**1.0**	11.0	11.4	10.9	10.6	11.3	**11.0**	**0.3**
0	**80**	**2**	28.1	36.6	27.4	25.0	34.5	**30.3**	**5.0**	-51.0	-53.5	-53.9	-48.5	-57.2	**-52.8**	**3.3**	31.4	31.3	31.6	32.5	31.2	**31.6**	**0.5**
2	**80**	**1**	100.0	120.5	99.8	106.2	110.9	**107.5**	**8.6**	-2.3	-2.3	-2.5	-0.9	-3.1	**-2.2**	**0.8**	11.6	12.0	11.9	11.2	11.4	**11.6**	**0.3**
2	**80**	**2**	30.0	38.1	32.0	32.0	31.3	**32.7**	**3.1**	-58.0	-58.5	-60.2	-53.5	-60.7	**-58.2**	**2.8**	30.4	30.2	29.4	31.3	30.8	**30.4**	**0.7**
4	**80**	**1**	100.7	106.9	84.7	94.4	97.2	**96.8**	**8.2**	-3.4	-3.3	-3.3	-1.8	-3.4	**-3.0**	**0.7**	13.5	14.1	14.4	11.8	12.9	**13.4**	**1.0**
6	**80**	**1**	87.4	90.6	72.2	84.8	78.3	**82.7**	**7.4**	-3.3	-3.2	-2.7	-1.6	-3.1	**-2.8**	**0.7**	12.6	12.5	13.0	11.5	11.5	**12.2**	**0.7**
8	**80**	**1**	62.3	69.3	54.0	71.7	59.5	**63.4**	**7.2**	-2.7	-2.6	-2.2	-0.7	-2.6	**-2.1**	**0.9**	12.5	12.3	12.8	10.8	11.5	**12.0**	**0.8**
10	**80**	**1**	44.4	48.0	40.2	51.0	38.6	**44.5**	**5.2**	-2.6	-3.0	-2.1	-0.1	-2.5	**-2.1**	**1.2**	12.3	13.7	13.0	10.3	11.7	**12.2**	**1.3**
12	**80**	**1**	29.1	35.9	29.3	33.6	27.0	**31.0**	**3.7**	-3.0	-3.5	-2.7	0.0	-2.7	**-2.4**	**1.4**	12.5	15.2	12.4	11.1	12.6	**12.8**	**1.5**
14	**80**	**1**	22.6	25.4	22.1	23.1	22.0	**23.0**	**1.4**	-2.7	-4.7	-2.1	-0.6	-2.3	**-2.5**	**1.5**	11.9	18.4	13.1	11.1	11.2	**13.1**	**3.0**
16	**80**	**1**	19.4	22.4	15.5	17.4	16.1	**18.1**	**2.8**	-1.9	-3.1	-1.8	-2.1	-3.2	**-2.4**	**0.7**	11.8	14.4	16.8	12.5	13.4	**13.8**	**2.0**
18	**80**	**1**	16.6	18.9	16.8	13.9	13.8	**16.0**	**2.2**	-2.5	-4.7	-1.8	-1.5	-3.1	**-2.8**	**1.3**	13.4	19.0	16.8	16.9	12.3	**15.7**	**2.8**
20	**80**	**1**	13.0	13.6	13.2	11.6	12.7	**12.8**	**0.8**	-3.4	-4.6	-0.7	-1.8	-4.1	**-2.9**	**1.6**	14.4	36.9	15.6	17.6	9.9	**18.9**	**10.5**
22	**80**	**1**	10.9	13.9	9.9	10.6	9.8	**11.0**	**1.7**	-4.7	-5.8	-0.1	-1.1	-5.0	**-3.3**	**2.5**	16.6	22.5	16.8	18.0	13.5	**17.5**	**3.3**
24	**80**	**1**	10.4	9.9	9.1	11.2	10.6	**10.2**	**0.8**	-3.7	-2.2	-2.7	-3.1	-4.8	**-3.3**	**1.0**	15.6	16.8	19.7	21.9	10.7	**16.9**	**4.3**
26	**80**	**1**	9.6	9.1	8.8	12.0	8.7	**9.6**	**1.4**	-5.0	-2.7	-2.6	-2.0	-4.5	**-3.3**	**1.3**	15.1	19.7	23.3	19.7	10.2	**17.6**	**5.0**
28	**80**	**1**	9.8	7.9	11.8	7.0	8.5	**9.0**	**1.9**	-6.0	-1.0	-5.4	-2.3	-3.7	**-3.7**	**2.1**	15.6	36.1	10.9	28.8	33.7	**25.0**	**11.2**
30	**80**	**1**	9.7	8.0	12.6	8.4	10.5	**9.8**	**1.9**	-5.7	-2.2	-5.3	-3.6	-4.3	**-4.2**	**1.4**	15.0	28.9	10.6	15.7	32.8	**20.6**	**9.7**

Above are details of all the data extracted from spectra for observations made for varying Galactic latitudes.

References

M Abramowitz and I Stegun. *Handbook of Mathematical Functions: with Formulas, Graphs, and Mathematical Tables*. Courier Dover Publications, 2012.

O Agertz, G Lake, R Teyssier, B Moore, L Mayer, and AB Romeo. Large-Scale Galactic Turbulence: Can Self-Gravity Drive The Observed HI Velocity Dispersions? *Monthly Notices of the Royal Astronomical Society*, 392(1):294–308, 2009.

J Binney and S Tremaine. *Galactic Dynamics*. Princeton University Press, 1987.

WB Burton. The Large-Scale Distribution of Neutral Hydrogen in the Galaxy. In *Galactic and Extra-Galactic Radio Astronomy*, pages 82–117. Springer, 1974.

IB Cohen and A Whitman. *Isaac Newton. The Principia. Mathematical Principles of Natural Philosophy. A New Translation*. University of California Press, 1999.

D Dahlin. Reducing data from SALSA in Matlab: SalsaSpectrum v1.6. 2013.

H Ewen and E Purcell. Observation of a Line in the Galactic Radio Spectrum. *Nature*, 168 (4270):356–358, 1951.

KM Ferriere. The Interstellar Environment of our Galaxy. *Reviews of Modern Physics*, 73(4): 1031, 2001.

KC Freeman. On the Disks of Spiral and SO Galaxies. *The Astrophysical Journal*, 160:811, 1970.

IS Gradshteyn and IM Ryzhik. *Table of Integrals, Series, and Products*, volume 6. Academic Press New York, 1965.

C Horellou and D Johansson. Hands-On Radio Astronomy Mapping the Milky Way. 2013.

P Kalberla and L Dedes. Global Properties of the HI Distribution in the Outer Milky Way. *arXiv preprint arXiv:0804.4831*, 2008.

P Kalberla and J Kerp. The HI Distribution of the Milky Way. *Annual Review of Astronomy and Astrophysics*, 47:27–61, 2009.

S Kent. Dark Matter in Spiral Galaxies. I - Galaxies with Optical Rotation Curves. *The Astronomical Journal*, 91:1301–1327, 1986.

K Lang. *Astrophysical Formulae*, volume 1. Springer, 1999.

ES Levine, C Heiles, and L Blitz. The Milky Way Rotation Curve and Its Vertical Derivatives: Inside the Solar Circle. *The Astrophysical Journal*, 679(2):1288–1298, 2008.

N McClure-Griffiths, D Pisano, M Calabretta, H Ford, F Lockman, L Staveley-Smith, P Kalberla, J Bailin, L Dedes, S Janowiecki, et al. GASS: The Parkes Galactic All-Sky Survey. I. Survey Description, Goals, and Initial Data Release. *The Astrophysical Journal Supplement Series*, 181(2):398, 2009.

Y Sofue. Mass Distribution and Rotation Curve in the Galaxy. In *Planets, Stars and Stellar Systems*, pages 985–1037. Springer, 2013.

RJ Tayler. *Galaxies: Structure and Evolution*. Cambridge University Press, 1993.